

Comparing the latent features of universal machine-learning interatomic potentials

Sofia Chorna,¹ Davide Tisi,¹ Cesare Malosso,¹ Wei Bin How,¹ Michele Ceriotti,^{1,*} and Sanggyu Chong^{1,†}

¹*Laboratory of Computational Science and Modeling, Institut des Matériaux, École Polytechnique Fédérale de Lausanne, 1015 Lausanne, Switzerland*

(Dated: January 23, 2026)

Abstract

The past few years have seen the development of “universal” machine-learning interatomic potentials (uMLIPs) capable of approximating the ground-state potential energy surface across a wide range of chemical structures and compositions with reasonable accuracy. While these models differ in the architecture and the dataset used, they share the ability to compress a staggering amount of chemical information into descriptive latent features. Herein, we systematically analyze what the different uMLIPs have learned by quantitatively assessing the relative information content of their latent features with feature reconstruction errors, and observing how the trends are affected by the choice of training set and training protocol. We find that uMLIPs encode the chemical space in significantly distinct ways, with substantial cross-model feature reconstruction errors. When variants of the same model architecture are considered, trends become dependent on the dataset, target, and training protocol of choice. We also observe that fine-tuning of a uMLIP retains a strong pre-training bias in the latent features. Finally, we discuss how atom-level features, which are directly output by MLIPs, can be compressed into global structure-level features via concatenation of progressive cumulants, each adding significantly new information about the variability across the atomic environments within a given system.

* michele.ceriotti@epfl.ch

† sanggyu.chong@epfl.ch

I. INTRODUCTION

Machine learning (ML) has brought transformative changes to the field of computational materials science. Data-driven algorithms enable simulations and electronic structure calculations with near *ab initio* accuracy to reach unprecedented length and time scales [1–7]. A particularly active frontier in this field is the development of “universal” machine-learned interatomic potentials (uMLIPs) that aim for applicability across the entire chemical composition space [8–15]. Such models alleviate the need for laborious dataset construction and model training from scratch, and instead allow zero-shot deployment or fine-tuning of existing uMLIPs, further accelerating applications across diverse areas of chemistry and materials science.

To date, several dozens of uMLIPs have been developed, each employing distinct atomic descriptors, neural network (NN) architectures, and training datasets of varying scope and composition [16–25]. Despite their rapidly growing diversity, most uMLIPs have been evaluated primarily on curated benchmarking suites that assess their accuracy across standard material modeling tasks [26–28]. This limited perspective motivates a deeper examination of the similarities and differences among uMLIPs, particularly how they represent and interpret the chemical space [29].

Regardless of their architectural details, all uMLIPs share a key characteristic: they encode the multidimensional description of atomic systems, comprised of types and positions of constituent atoms, into a compact latent representation containing only a few hundred features. These latent representations embody the distinct ways in which different uMLIPs perceive and organize the chemical space, and the utility of these latent features has been demonstrated in various contexts: uncertainty quantification [30–35], outlier detection [36, 37], active learning [33, 38, 39], dataset curation [40–42], and system classification [43, 44].

In this work, we leverage the latent features of uMLIPs to systematically and quantitatively analyze the similarities and differences in how these models perceive and structure the chemical space. While recent complementary works have focused on discerning whether there exists a converged or aligned representation of matter across the uMLIPs [45, 46], here we adopt a purely statistical approach, using the global and local feature reconstruction errors of Goscinski *et al.* [47] to assess the information content across the latent features of four uMLIPs: MACE-MP-0b3 [10], PET-MAD [13], DPA-3.1 [8], and UMA-S-1P1 [9]. We

investigate the mutual reconstructability of the uMLIP latent features, as well as those of model variants trained with different datasets and training strategies. We also extend the evaluation to the latent features of PET-MAD and those of PET-MAD-DOS [48], a model with nearly identical architecture and dataset but trained for a different target property. We then study the evolution of the latent space during fine-tuning, and explore how the atomic latent features can be efficiently aggregated into global features from the information content standpoint.

We find that all uMLIPs uniquely encode chemical space with significant cross-model reconstruction errors, where some models are more accurately linearly reconstructed by others. When considering the variants of model architectures targeting different datasets, we observe that single-task models (MACE-MP-0b3) and multi-task models (MACE-mh-1 [11], DPA-3.1) share relatively consistent representations across datasets, while the mixture of linear experts (MoLE) model (UMA-S-1P1) specializes the features far more distinctly. We observe that the information content of “last-layer” and “backbone” features in a model architecture is similar, yet the backbone features encode more information than last-layer features cannot reconstruct. We also demonstrate that fine-tuning of the uMLIP exhibits a strong pre-training bias in the latent feature space. Finally, we demonstrate the compression of local, atom-level features into global, structure-level features by concatenating their progressive cumulants, resulting in an information-rich structural descriptor that obeys desirable scaling laws and preserves the knowledge of configurational inhomogeneity.

II. METHODS

For our analysis, we mainly consider MACE-MP-0b3, PET-MAD, DPA-3.1, and UMA-S-1P1, which constitute a non-exhaustive yet diverse set of uMLIPs that differ vastly in their message-passing NN architectures, learning strategies, and training datasets (see Table I). MACE-MP-0b3 [10] is built on an $E(3)$ -equivariant message-passing NN that constructs higher body-order correlations using equivariant tensor products and body-ordered polynomials. PET-MAD [13] is based on a rotationally unconstrained transformer-based graph neural network (GNN), where strict geometrical equivariance is not enforced by architecture but is effectively learned through rotational data augmentation during training [49]. DPA-3.1 [8] is an attention-based model of the Deep Potential (DP) family [50] that produces

TABLE I. Key characteristics of the uMLIPs considered in this work. Dataset sizes are reported by the number of structures. For UMA-S-1P1, 6M denotes the active parameters used per structure during inference, while 150M is the total across all the experts.

	MACE-MP-0b3	PET-MAD	DPA-3.1	UMA-S-1P1
Training strategy	Single model	Single model	Multi-task model	Mixture of linear experts model
Dataset(s)	MPtrj (1.58M) [16]	MAD (0.096M) [18]	OpenLAM-v1 (163M) [15]	OMat24, OC20, ODAC25, OMC25, OMol25 (total 569M) [21–25]
Equivariance	E(3)-equivariant	Rotationally unconstrained; equivariance learned by data augmentation	SE(3)-invariant	E(3)-equivariant
# of parameters	4.69M	3.3M	3.26M	6M (active), 150M (total)
Feature dim.	144	512	240	128
Cutoff (Å)	6.0	4.5	6.0	6.0

fully rotation- and translation-invariant atomic descriptors via a gated attention mechanism. UMA-S-1P1 [9] is implemented upon a large-scale E(3)-equivariant mixture-of-experts architecture built on the eSEN [51] backbone that uses a MoLE design. For UMA-S-1P1 and DPA-3.1, which are a MoLE model and a multi-head model, respectively, we use the expert or the head corresponding to the OMat24 dataset [23], given that MACE-MP-0b3 and PET-MAD have been trained on similar materials-oriented datasets.

We define the latent features of each uMLIP as the tokens extracted from a given layer of the model architecture. These features have been processed through multiple layers of message-passing to encode the information aggregated from neighboring atoms within the defined cutoff radius. We primarily focus on the last-layer features, corresponding to

the representation most refined for the regression task obtained after all message-passing iterations and subsequent multilayer perceptron (MLP) transformations. Since all considered uMLIPs adopt a locality ansatz, we extract atomic features $\xi(A_i)^F$ for each atom i in structure A via a forward-pass through the model F .

To enable a consistent, scale-invariant comparison across the models, the features are centered to zero mean and globally scaled so that their total variance across all dimensions equals one on the analysis dataset for each uMLIP, thereby preserving the relative scales between feature dimensions.

A. Feature space comparison metrics

In our analysis, we primarily take a *quantitative* approach in studying the similarities and differences between the latent space of uMLIPs. To this end, we compute the global feature reconstruction error (GFRE) and the local feature reconstruction error (LFRE) proposed by Goscinski *et al.* [47]. These metrics assess the relative expressive power of feature spaces by determining how well one set of features can reconstruct another.

Let \mathcal{D} be a set of n atomic environments. For two models F and F' , their feature matrices are first computed:

$$X_{\mathcal{D}}^F = \begin{bmatrix} \xi_1^F \\ \xi_2^F \\ \vdots \\ \xi_n^F \end{bmatrix} \in \mathbb{R}^{n \times d_F}, \quad X_{\mathcal{D}}^{F'} = \begin{bmatrix} \xi_1^{F'} \\ \xi_2^{F'} \\ \vdots \\ \xi_n^{F'} \end{bmatrix} \in \mathbb{R}^{n \times d_{F'}}, \quad (1)$$

where d_F and $d_{F'}$ denote the dimensionalities of the feature vectors for models F and F' , respectively, which do not need to be equal.

To compute the GFRE, we determine the optimal linear mapping $\hat{P}_{FF'} \in \mathbb{R}^{d_F \times d_{F'}}$ that minimizes the reconstruction loss over a training set $\mathcal{D}_{\text{train}}$:

$$\hat{P}_{FF'} = \arg \min_{\hat{P}} \left\| X_{\mathcal{D}_{\text{train}}}^{F'} - \hat{P} X_{\mathcal{D}_{\text{train}}}^F \right\|_F^2, \quad (2)$$

where $\|\cdot\|_F$ denotes the Frobenius norm that measures the overall square differences between two matrices, i.e., total Euclidean distances between all pairs of atomic feature vectors.

After obtaining the optimized $\hat{P}_{FF'}$, the GFRE is computed for $\mathcal{D}_{\text{test}}$ as the root mean square error (RMSE) between $X_{\mathcal{D}_{\text{test}}}^{F'}$ and $\hat{P}_{FF'}X_{\mathcal{D}_{\text{test}}}^F$:

$$\text{GFRE}_{\mathcal{D}_{\text{test}}}(F, F') = \sqrt{\frac{\|X_{\mathcal{D}_{\text{test}}}^{F'} - \hat{P}_{FF'}X_{\mathcal{D}_{\text{test}}}^F\|_F^2}{|\mathcal{D}_{\text{test}}|}}, \quad (3)$$

where $|\mathcal{D}_{\text{test}}|$ is the total number of atomic environments in the test set $\mathcal{D}_{\text{test}}$. A low GFRE indicates that the latent features of F contain sufficient information to linearly reconstruct the latent features of F' , meaning that both models encode similar information about the atomic environments. In contrast, a large value signifies that features of F' carry supplementary information that cannot be recovered as a linear transformation of the features of F . The GFRE mapping is directional, i.e., $\text{GFRE}(F, F') \neq \text{GFRE}(F', F)$.

As the GFRE exclusively targets linear transformations between the features, it overlooks potential nonlinear mapping between the feature spaces. The LFRE is an alternative metric that indirectly addresses this limitation: it quantifies how well a *local* neighborhood in one feature space can be reconstructed from its corresponding neighborhood in another.

For each test environment $i \in \mathcal{D}_{\text{test}}$, we identify its k nearest neighbors in the training set $\mathcal{D}_{\text{train}}$ according to the Euclidean distance in feature space F . Collectively, these neighbor indices are $\mathcal{N}_i^F = \{j_1, \dots, j_k\} \subset \mathcal{D}_{\text{train}}$. For these neighbors, we denote source-space and target-space features as:

$$X_{\mathcal{N}_i^F}^F = \begin{bmatrix} \boldsymbol{\xi}_{j_1}^F \\ \boldsymbol{\xi}_{j_2}^F \\ \vdots \\ \boldsymbol{\xi}_{j_k}^F \end{bmatrix} \in \mathbb{R}^{k \times d_F}, \quad X_{\mathcal{N}_i^F}^{F'} = \begin{bmatrix} \boldsymbol{\xi}_{j_1}^{F'} \\ \boldsymbol{\xi}_{j_2}^{F'} \\ \vdots \\ \boldsymbol{\xi}_{j_k}^{F'} \end{bmatrix} \in \mathbb{R}^{k \times d_{F'}}. \quad (4)$$

To restrict the learning problem to modeling only relative displacements on the local manifold patch, each neighborhood is centered by subtracting its mean:

$$\tilde{X}_{\mathcal{N}_i^F}^F = X_{\mathcal{N}_i^F}^F - \bar{\boldsymbol{\xi}}_{\mathcal{N}_i^F}^F, \quad \tilde{X}_{\mathcal{N}_i^F}^{F'} = X_{\mathcal{N}_i^F}^{F'} - \bar{\boldsymbol{\xi}}_{\mathcal{N}_i^F}^{F'}. \quad (5)$$

A local linear map is then fitted to align the centered neighborhood of these k training points from F to F' :

$$\hat{P}_i^{FF'} = \arg \min_{\hat{P}} \left\| \tilde{X}_{\mathcal{N}_i^F}^{F'} - \hat{P} \tilde{X}_{\mathcal{N}_i^F}^F \right\|_F^2. \quad (6)$$

This local neighborhood mapping is then applied to reconstruct the centered feature of the test point i itself:

$$\hat{\boldsymbol{\xi}}_i^{F'} = \bar{\boldsymbol{\xi}}_{\mathcal{N}_i^F}^{F'} + \hat{P}_i^{FF'}(\boldsymbol{\xi}_i^F - \bar{\boldsymbol{\xi}}_{\mathcal{N}_i^F}^F). \quad (7)$$

Finally, the LFRE is the RMSE over all test environments:

$$\text{LFRE}_{\mathcal{D}_{\text{test}}}(F, F') = \sqrt{\frac{\sum_{i \in \mathcal{D}_{\text{test}}} \left\| \boldsymbol{\xi}_i^{F'} - \hat{\boldsymbol{\xi}}_i^{F'} \right\|_2^2}{|\mathcal{D}_{\text{test}}|}}. \quad (8)$$

The neighborhood size k can be optimized, but here we set it to the smaller feature dimension between the two models for simplicity. Low LFRE values show that the local structure of F' can be reconstructed by F , hence the two feature spaces contain similar information, even if they differ globally.

We clarify that the definitions of “global” and “local” in the context of feature reconstruction errors do not correspond to the usual atomic versus system-wide considerations in atomistic ML (see SI V for a schematic overview). Rather, “global” denotes a single linear transformation applied across the entire dataset of atomic features, whereas “local” involves fitting separate linear mappings for localized neighborhoods within the high-dimensional feature space. Both metrics can operate on both atomic-level and structure-level features, but differ in how they assess reconstructability across the feature manifold.

Owing to the feature normalization, both the GFRE and LFRE are usually bounded between 0 and 1, with 0 signifying perfect linear reconstruction, thus comparable information between the feature spaces. However, the upper bounds can be exceeded in case of reconstruction failure due to ill-conditioned linear mappings, which indicates large dissimilarity or incompatibility between the feature spaces. For our analysis, we use the GFRE and LFRE implementations in *scikit-matter* [52] with ridge regression and default 2-fold cross-validation to determine the ridge regularization, with regularization α values scanned over a logarithmic range from 10^{-9} to 1, and the final value was selected as the smallest α that provided numerical stability.

B. Feature space projection

In a few examples, we complement this quantitative analysis by a visual mapping of the uMLIP features to a lower-dimensional space using Principal Covariates Regression (PCovR)

[53, 54]. This dimensionality reduction technique interpolates between two objective functions: maximizing variance retention in the original features via principal component analysis (PCA), and optimizing linear regression performance on a target property. In our context, by mixing in the regression term in addition to the PCA term, we gently enforce a degree of consistency across the maps produced for different models to aid interpretation.

Given a set of high-dimensional feature matrix $X \in \mathbb{R}^{n \times d}$ and target property matrix $Y \in \mathbb{R}^{n \times p}$, PCovR determines a latent space projection $\mathbf{T} \in \mathbb{R}^{n \times k}$ that minimizes the loss:

$$\mathcal{L} = \alpha \|X - \hat{X}\|_F^2 + (1 - \alpha) \|Y - \hat{Y}\|_F^2, \quad (9)$$

where $\hat{X} = \mathbf{T}P_X^\top$ is the approximation of the original feature space X (PCA term) and $\hat{Y} = \mathbf{T}P_Y^\top$ is the prediction of targets (linear regression term). The matrices P_X and P_Y represent projection weights that map latent coordinates back to the original feature and target dimensions. The interpolation between the two terms is controlled by a tunable parameter $\alpha \in [0, 1]$. In our analysis, we use *scikit-matter* implementation with $\alpha = 0.5$ and $k = 2$ principal components.

To prepare the inputs, atomic features are aggregated to the structure-level by computing the cumulants introduced in Sec. III F across atoms within each structure. The target property Y is defined as the cohesive energies per atom, calculated by subtracting an atomic baseline energy from the reference total potential energy of each structure and normalizing by the number of atoms.

III. RESULTS

A. Latent feature comparison between uMLIPs

We first quantitatively compare the latent features of different uMLIPs by computing the GFRE and LFRE between the four models considered. The errors are computed for structures in the test subset of the Massive Atomic Diversity (MAD) dataset [18], which contains chemical systems with a broad coverage across 85 elements and exhibits vast structural diversity. We exclude the single-atom structures (incompatible with UMA) and polonium- or radon-containing structures (not supported by MACE trained on MPtrj) to yield 258,561 atomic environments from 9,461 structures. We then perform random stratified sampling across the subsets of MAD dataset at the atomic level to select 1,000 atomic environments

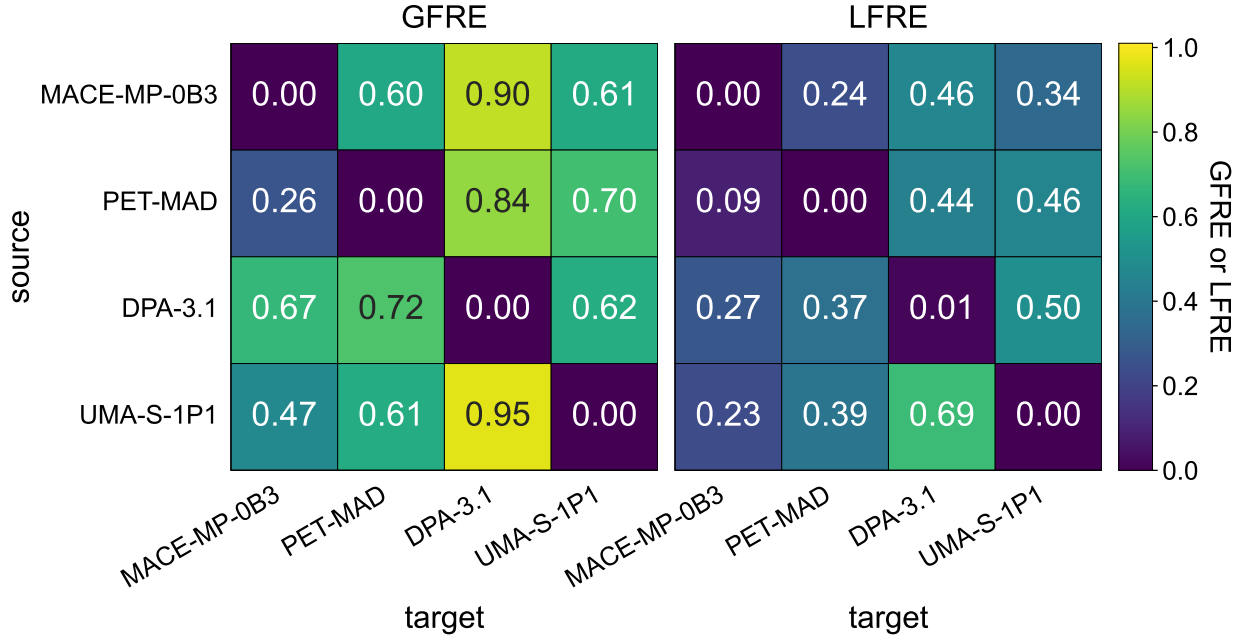


FIG. 1. Heat maps of the global feature reconstruction error (GFRE, left) and local feature reconstruction error (LFRE, right) for the atomic last-layer latent features of MACE-MP-0b3, PET-MAD, DPA-3.1, and UMA-S-1P1, computed for the atomic environments from the test subset of the MAD dataset. Each cell represents the reconstruction error when mapping latent features of the “source” (row) to “target” (column).

for $\mathcal{D}_{\text{test}}$. All remaining environments are used as $\mathcal{D}_{\text{train}}$ to compute the regression weights $\hat{P}_{FF'}$.

The heat maps in Fig. 1 reveal distinct trends in the feature reconstruction performances across the uMLIPs. Overall, the values are large (average of 0.66 for GFRE and 0.37 for LFRE off-diagonal cross-terms), indicating that each model encodes the chemical space in a unique manner. That latent spaces of different models differ significantly is not surprising. Latent features are only weakly constrained by the learning target: in principle, a model could learn the energy as the first feature, and have all others reflect completely unrelated components of the molecular structure. Therefore, the latent space reflects the priors explicitly and implicitly encoded in the model architecture, the choice of hyperparameters, and the training strategy.

The LFREs are generally lower than the GFREs, which reflects the ability of the LFRE to implicitly account for nonlinear relationships between the feature spaces. The lowest GFREs

and LFREs are observed when MACE-MP-0b3 features are used as targets, suggesting that the other uMLIPs can reliably recover the information encoded in its features. Conversely, the highest errors are observed when DPA-3.1 features serve as targets. The average GFREs across the off-diagonal targets for each source model are 0.70 for MACE-MP-0b3, 0.60 for PET-MAD, 0.67 for DPA-3.1, and 0.68 for UMA-S-1P1. For the LFRE, they are 0.35, 0.33, 0.38, and 0.44, respectively. PET-MAD exhibits marginally lower GFREs and LFREs in reconstructing the features of all other uMLIPs, despite being trained on the smallest dataset among the models considered. To rule out the fact that the low PET-MAD reconstruction errors are lower only because we are using the MAD dataset as a benchmark, we repeat the analysis using the Alexandria subset [17] (cf. SI VI). We observe similar trends, indicating that the smaller MAD dataset can still sufficiently represent the configuration space of much larger datasets, and that its choice for our analysis does not introduce a significant bias.

In SI VII, we also present the feature reconstruction errors (FREs) across the models for the backbone features (representations obtained immediately after message-passing and before the MLP readout), which show smaller reconstruction error (average off-diagonal GFRE is 0.54, LFRE is 0.30) and hence relatively higher generalizability across the models.

B. Comparing model variants

Beyond the comparison between entirely different uMLIPs, we assess the consistency of information content across uMLIP “variants” of the same architecture. Through this analysis, we establish the sensitivity of various architectures to changes in the training dataset or target. We also establish a scale for the “internal” variability of each architecture that helps calibrate the comparison between models that differ more substantially. We categorize the variants into: “single-task” models where an entirely separate model architecture is trained from scratch for distinct datasets, and “multi-task” models that either adopt a multi-head [55, 56] or mixture-of-experts [57–59] approach to simultaneously target multiple datasets with a single model architecture, often with significant weight sharing between the prediction tasks.

We first compare the reconstruction errors across the single-task MACE variants, which have been trained separately on MPtrj [16], OMat24 [23], MatPES-PBE, and MatPES-r2SCAN [19]. The latter two datasets only differ in the exchange-correlation functional used

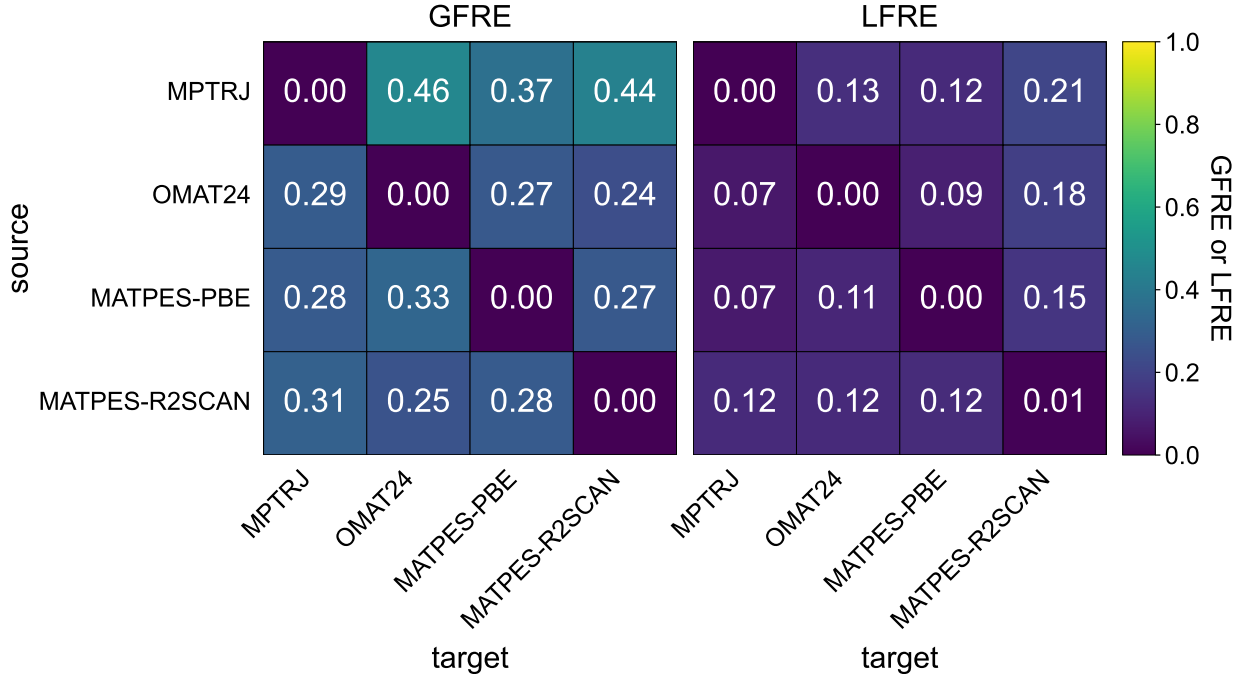


FIG. 2. The reconstruction errors across single-task MACE models trained on MPtrj (MACE-MP-0b3), OMat24, and MatPES (PBE and r2SCAN) datasets [16, 19, 23] evaluated on the MAD test subset.

during the reference calculations, which are PBE [60] and r2SCAN [61], respectively. Overall, the reconstruction errors are moderately low across the variants (Fig. 2) (the average off-diagonal GFRE is 0.31, and the average LFRE is 0.12). The MPtrj variant exhibits the largest overall GFREs and LFREs (average GFRE and LFRE are 0.42 and 0.15, respectively), which reflects the limited information content of the smallest and oldest MPtrj dataset. The reconstruction errors between MatPES-PBE and MatPES-r2SCAN are comparable to the other cases, revealing that having different functionals in the reference calculations converges the resulting variant models into significantly distinct latent spaces. The lowest overall errors are observed for the OMat24 variant (on average, the GFRE is 0.25 and the LFRE is 0.09), which is indicative of the relatively rich information content of OMat24 dataset that is often utilized in the pre-training of uMLIPs [11, 23, 51, 62, 63].

In DPA-3.1, a model trained on the OpenLAM-v1 collection of 31 datasets [15], the following multi-task learning strategy is adopted: the model incorporates a shared backbone network while still being conditioned for different datasets via one-hot encoding. This backbone is followed by multiple specialized output heads, or branches, tailored to each

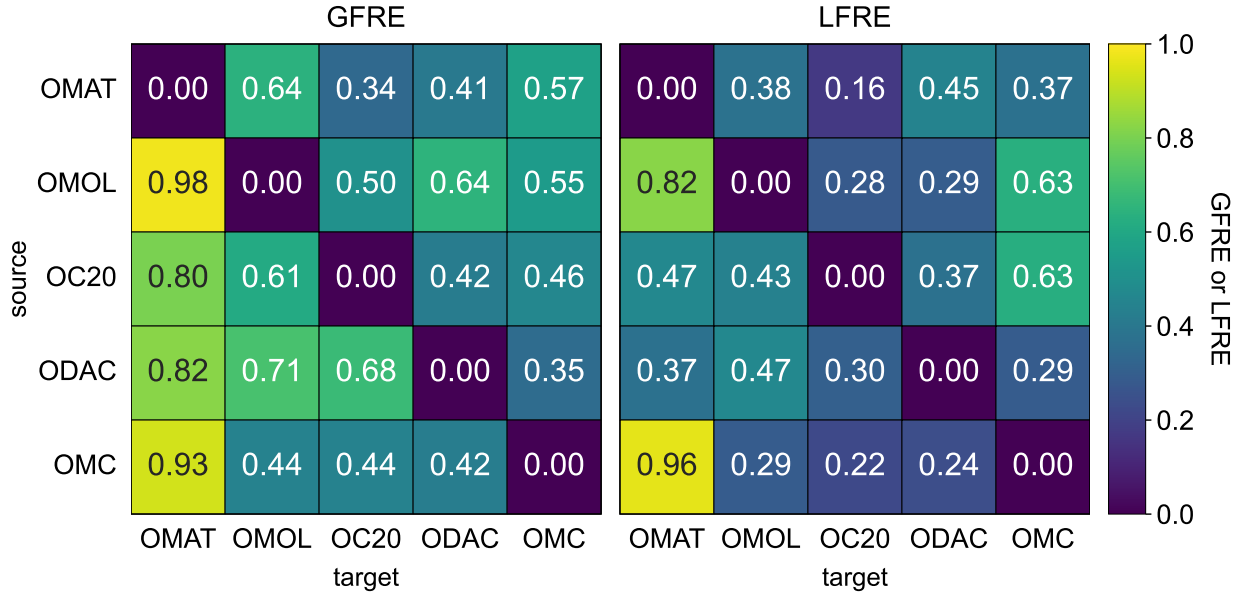


FIG. 3. The reconstruction errors across different input tasks of UMA-S-1P1 trained on OMat24, OMOL, OC20, ODAC, and OMC [21–25] evaluated on the MAD test subset.

dataset [8]. Reconstruction results between branches corresponding to OMat24, MPtrj, OC20, ODAC, and SPICE datasets [16, 20–23], presented in SI VIII A 1, indicate comparable latent space consistency to the MACE single-task models, suggesting that strong parameter sharing without dynamic routing preserves highly universal latent representations.

UMA is a uMLIP developed with the goal of having a single model that performs well across all atomistic modeling tasks, encompassing materials, molecules, and their interactions. To do so, the model has been trained simultaneously on OMol25, OMat24, OC20, ODAC25, and OMC25 [21–25]. Instead of adopting a multi-head approach for the different datasets, the model incorporates a MoLE strategy in its interaction layers, where the weights of the different experts are computed based on the global embedding that encodes the dataset-specific information [9]. UMA-S-1P1 shows greater variability in reconstruction errors (see Fig. 3), which suggests that the MoLE mechanism encourages stronger specialization of feature manifolds corresponding to each dataset. We observe that the OMat24 task reconstructs other variants with relatively low errors (average off-diagonal GFRE is 0.49 and LFRE is 0.34), similar to previous results with MACE, whereas other variants struggle to approximate its latent space linearly. We also observe group-level consistency, as the features of catalysis-related tasks (OC20, ODAC25, OMC25) generally exhibit lower

reconstruction errors (GFRE is 0.46, and LFRE is 0.34 on average across this group).

To investigate the influence of the training domain on the learned latent space, we also compare the organics-focused MACE-OFF23 model [64] with the materials-focused MACE-MP-0b3 [10] by evaluating the reconstruction errors on the organic structures of the MAD test subset. As detailed in SI VIII B (Table S2), the materials-trained model reconstructs the organic-trained model almost perfectly (GFRE is 0.02), whereas the reverse direction yields remarkably higher global error (GFRE is 0.36), despite similar local agreement (LFRE is 0.04). This could suggest that the broader materials manifold learned by MACE-MP-0b3 cannot be fully captured by MACE-OFF23, which has been exposed only to organic systems.

We further examine the effect of model capacity by comparing the MACE checkpoints of varying sizes (small, medium, large) within the same architecture family, for both the materials-focused MACE-MP-0a series and the organic-focused MACE-OFF23 series (SI VIII C, Fig. S6). Interestingly, regardless of size, all MACE-MP-0a variants reconstruct each other with near-perfect linear mapping, whereas reconstructing the large MACE-OFF23 checkpoint from its smaller counterparts is significantly harder (average GFRE is 0.48 when small/medium \rightarrow large). A similar size-scaling analysis on PET-OMAT models [65] (SI Fig. S7) shows that smaller models can still approximate the principal manifold of larger ones reasonably well, with the medium-sized variant offering a good information content/size tradeoff.

Finally, we assessed the impact of single-task versus multi-head readout architectures using two MACE models trained on the same OMat24 dataset: the original single-head MACE-OMAT-0 and the OMat-specific head of the multi-head MACE-MH-1 model [11] (the latter having undergone multi-head replay fine-tuning after initial pre-training). Results are presented in SI VIII D (Table S4). Both directions exhibit moderate global reconstruction error (GFRE is ~ 0.33) but low local error (LFRE is less than 0.10), demonstrating that the multi-head replay protocol preserves the core local feature neighborhoods of the original single-head representations while allowing the readout to become more expressive.

C. Varying targets

Although we have primarily focused on uMLIPs, universal models are also available for properties other than the ground state potential energy surface. To this end, we compare

the latent features of PET-MAD and PET-MAD-DOS [48]. The two models have nearly identical architectures, differing only in the last linear readout layer due to the different sizes of the targets (last-layer features are still of the same dimension), and are both trained on the MAD dataset. While PET-MAD was trained on energies and forces, PET-MAD-DOS was trained on the electronic density of states (DOS).

The results in SI IX reveal that PET-MAD-DOS exhibits more information content than PET-MAD, as seen by the lower GFRE and LFRE values (0.68 and 0.39 for energy \rightarrow DOS vs. 0.56 and 0.28 for DOS \rightarrow energy). While this observation is expected, provided that DOS contains far more information than the energies and forces, it is still interesting to see that the information content in the latent features also reflects our physical knowledge of the targets. Still, the substantial reconstruction error in the DOS \rightarrow energy direction indicates that the energy-based latent features also encode distinct information.

D. Fine-tuning

The advent of uMLIPs has made fine-tuning on domain-specific datasets a standard approach for obtaining accurate potentials tailored to specific applications that can still generalize well [1, 66–68]. Here, we analyze the reconstruction errors between features that arise from different fine-tuning strategies, as well as a model trained entirely from scratch. We also study the evolution of learned latent features along a “training trajectory” by computing the reconstruction errors of latent features sampled from model checkpoints at intermediate training epochs with respect to the fully trained model.

For our analysis, we consider the PET architecture and its pre-trained PET-MAD uMLIP as the baseline. We train material-specific MLIPs for lithium thiophosphate (LPS), a promising class of solid-state electrolytes widely studied for the next generation of battery materials [69–74]. We consider the following training or fine-tuning procedures: a bespoke model trained from scratch on the dataset from randomly initialized weights; full fine-tuning (FF), where all trainable model weights are optimized on the new dataset; “head-only” fine-tuning (HF), where only the weights of the MLP head are optimized during training while the rest remains fixed; full transfer learning (FTL), where a new MLP head is added with random weight initialization, and then all trainable weights of the model are optimized; head transfer learning (HTL), where a new MLP head is created with random weights, and

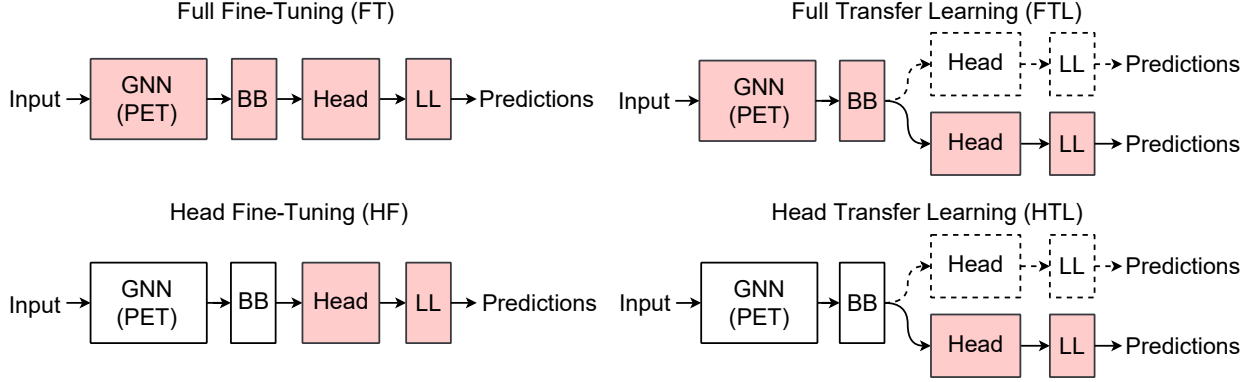


FIG. 4. A schematic overview of the fine-tuning strategies for the PET architecture: full fine-tuning, head fine-tuning, full transfer learning, and head transfer learning. The graph neural network (GNN) based on the Point Edge Transformer (PET) computes the backbone (BB) features. For a given prediction target, these BB features are fed into the readout “heads” (multi-layer perceptrons or MLPs) to generate the last-layer (LL) features. The four illustrated strategies involve training different combinations of these model components, and the trainable parts are colored in salmon.

only the MLP head weights are optimized. A schematic overview of the trainable parts for these fine-tuning strategies is given in Fig. 4. The training procedures were carried out using *metatrain* [75] (see SI X for the error metrics and hyperparameters of the fine-tuned models). We use the dataset from Ref. [76], which was previously used to model complex surface structural reconstructions on LPS. The dataset contains 4,088 structures, yielding 225,905 atomic environments in total. In particular, it contains the structures of bulk LPS in each of its phases (γ , β , α , and amorphous) and the structures of the LPS surface with and without absorbed water molecules.

Fig. 5 shows the reconstruction errors among the final models from the described fine-tuning strategies, the pre-trained PET-MAD model, and a bespoke PET model trained from scratch on the LPS dataset. The reconstruction errors are notably low between all of the fine-tuned models (FF, HF, FTL, and HTL) and the pre-trained PET-MAD model, which signifies a high degree of similarity in their last-layer features despite differences in training protocols. This suggests that the fine-tuned models retain a strong bias from the pre-trained model, which is also evident in the PCovR projections of the last-layer features (see Fig. S8). The bespoke model exhibits the highest reconstruction errors, yet the values are still moderate, revealing that its training has converged to a distinct yet nearby minima

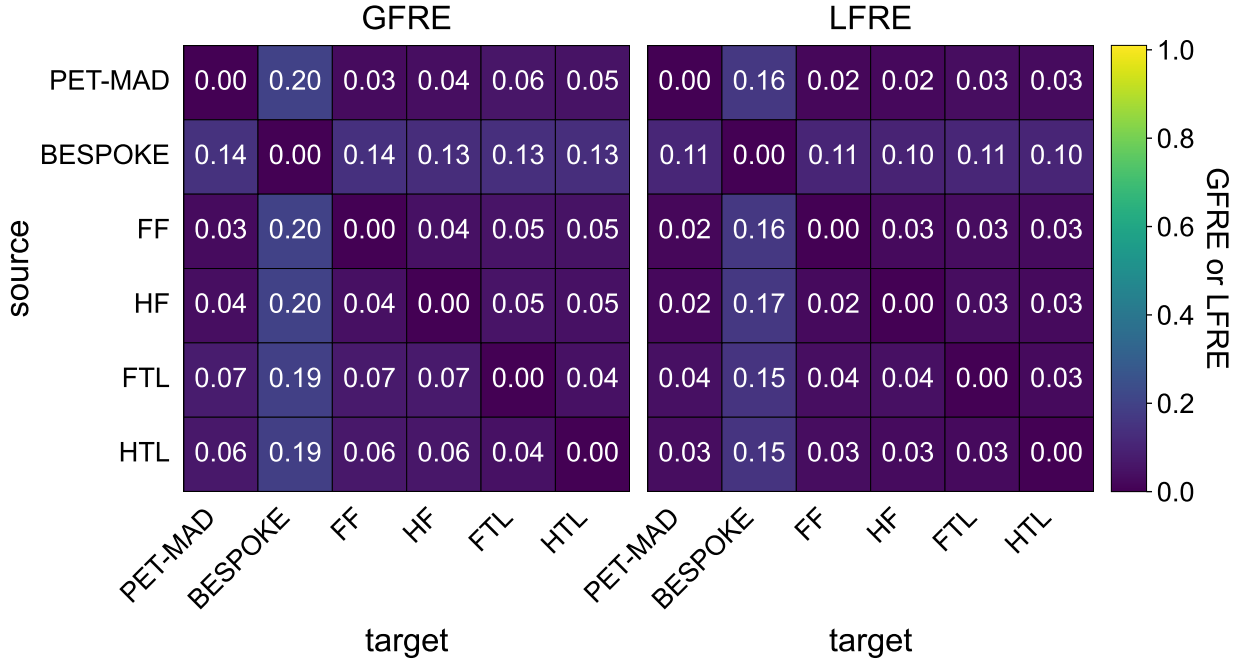


FIG. 5. The reconstruction errors across the last-layer atom-level features of differently fine-tuned PET checkpoints computed for the LPS dataset.

with respect to the other models.

Fig. 6 shows the evolution of the reconstruction errors along the training trajectory computed relative to the fully converged model for each strategy. The bespoke model trained from scratch starts with high GFRE and LFRE, which gradually decay, yet remain above numerical zero even after 1000 epochs (0.009 for GFRE and 0.005 for LFRE). In contrast, fine-tuned strategies begin with lower initial reconstruction errors due to pre-conditioning with the PET-MAD uMLIP, which then converge quickly to near-zero values. In FTL and HTL, the curve is not monotonic, and more than 400 epochs are needed for convergence, most likely due to the randomized head initialization. In HF, a similar number of epochs is needed to align the features with those of the final model, whereas FF converges the reconstruction errors to < 0.01 with only 20 epochs. This can be explained by the relative differences in the training degrees of freedom between the two strategies. Overall, the combination of low reconstruction errors in Fig. 5 and rapid convergence in Fig. 6 demonstrates that the last-layer features of PET-MAD provide a robust starting point for the fine-tuning strategies. This provides further explanation as to why the uMLIPs can converge rapidly to high accuracy when fine-tuned to a new, narrower dataset [68].

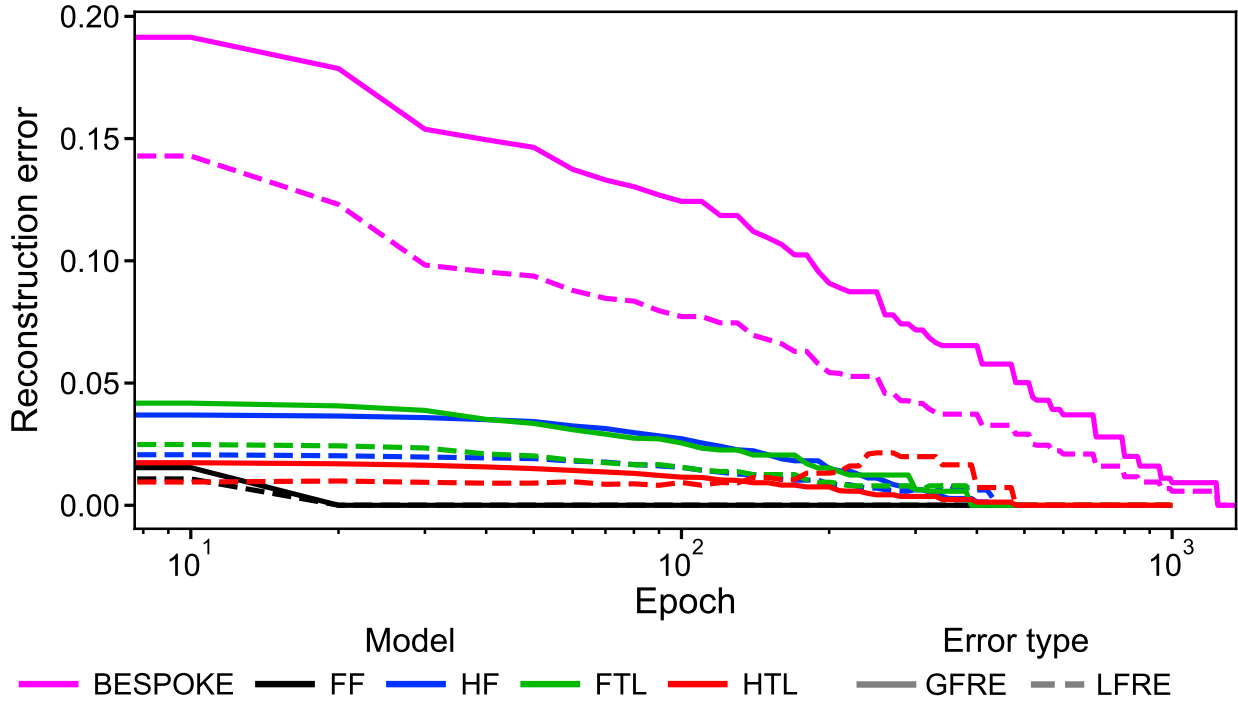


FIG. 6. The evolution of the reconstruction errors of last-layer atom-level features during training on the LPS dataset, where the errors have been computed with respect to the features of fully trained models corresponding to each respective fine-tuning strategy as targets.

E. Backbone vs. last-layer features

While we have chosen the last-layer (LL) features for our analysis thus far, the latent features can be extracted from any other layer within the NN architectures of the uMLIPs. Another features of particular interest are the “backbone” (BB) latent features, which correspond to the representations obtained immediately after all message-passing iterations, but before entering a multilayer perceptron (MLP) head, which is an architectural choice followed by many uMLIPs (see Fig. 4 for a sample schematic of PET-MAD). The BB features are of particular interest in multi-head and multi-task models, where they often serve as a shared input across the multiple heads. To provide examples of both multi-task and single-task contexts, we evaluate the reconstruction errors between the last-layer features and the backbone features for UMA and PET.

In UMA-S-1P1 (Fig. 7), the BB \rightarrow LL and LL \rightarrow BB GFREs are moderate and similar in both directions, consistent with the fact that a global linear mapping cannot capture the

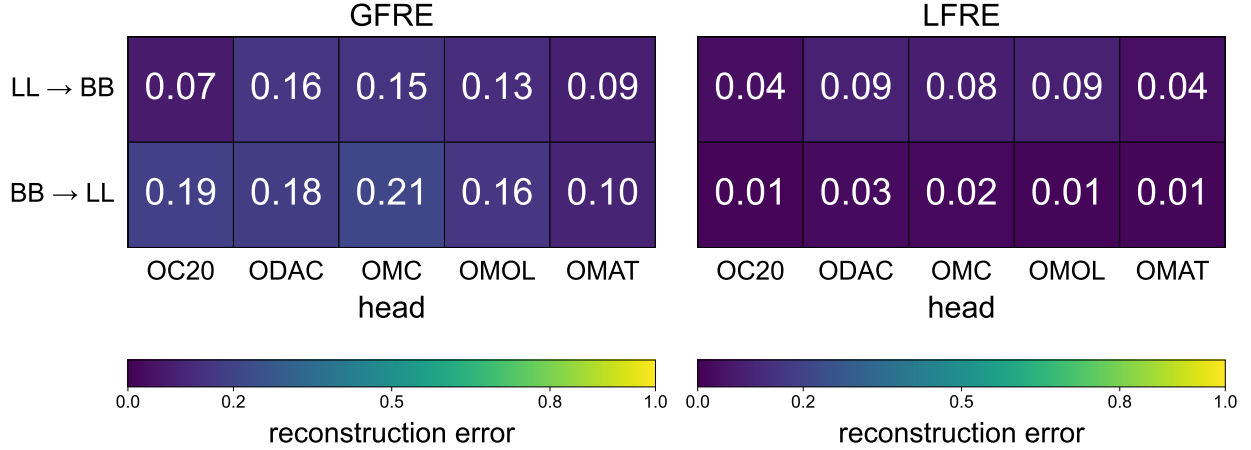


FIG. 7. The global and local reconstruction errors between the last-layer features (LL) and backbone features (BB) of UMA-S-1P1 for different experts, computed for the MAD test subset.

nonlinear effects of the MLP. On the contrary, the LFREs are lower, as they can locally capture the said transformation. The LL → BB LFRE is larger than vice versa, suggesting that there exists some information loss in going from the shared BB features to the specialized LL features, or equivalently, that the shared features contain more information, making them suitable for specialization into different prediction tasks.

For PET (Fig. S9 in SI XI), both reconstruction errors are higher and more varied across model variants compared to UMA-S-1P1, indicating greater divergence between BB and LL representations. Even in the GFRE, reconstructing BB from LL yields higher errors than the reverse case. Once again, the LFRE is lower in both reconstruction tasks, but the improvement is only minor in the case of LL → BB. We speculate that the large information loss might be associated with the MLP eliminating the non-invariant parts of the BB features, which takes place as the PET model learns the symmetries of the energy prediction task.

These asymmetries in the embedding reconstruction of the two uMLIPs highlight the dominant influence of model architecture on latent feature encodings, with design choices controlling the tradeoff between shared general-purpose representations and task-specific final refinements.

F. Local to global features

While most uMLIPs strictly work at the level of atom-centered local environments, one often needs to operate at the molecular or structural level, e.g., to build data-driven maps of datasets or to analyze the outcome of simulations [77, 78]. For these applications, it is customary to average the atomic descriptors to obtain global features [79, 80], which, however, entirely disregards the variability across the atomic environments and results in significant information loss. To mitigate this and capture comprehensive structural information, we investigate the use of higher-order cumulants of atomic features to construct structure-level descriptors.

To formalize this, consider a dataset \mathcal{D} consisting of structures, where each structure S has N_S atoms. For a given model F , the atomic feature matrix for a structure S is

$$X_S^F = \begin{bmatrix} \boldsymbol{\xi}_{S,1}^F \\ \boldsymbol{\xi}_{S,2}^F \\ \vdots \\ \boldsymbol{\xi}_{S,N_S}^F \end{bmatrix} \in \mathbb{R}^{N_S \times d_F}, \quad (10)$$

where $\boldsymbol{\xi}_{S,i}^F \in \mathbb{R}^{d_F}$ is the feature vector of the atom i in the structure.

We construct structure-level descriptors by concatenating the first M cumulants of the atomic feature distribution. Let $\boldsymbol{\kappa}_S^{(k)}$ denote k -th order cumulant vector for structure S . These are obtained from the central moments of the atomic features. Specifically, the mean feature vector is:

$$\bar{\boldsymbol{\xi}}_S^F = \frac{1}{N_S} \sum_{i=1}^{N_S} \boldsymbol{\xi}_{S,i}^F, \quad (11)$$

and for $k \geq 2$, the k -th central moment vector is:

$$\boldsymbol{\mu}_S^{(k)} = \frac{1}{N_S} \sum_{i=1}^{N_S} \left(\boldsymbol{\xi}_{S,i}^F - \bar{\boldsymbol{\xi}}_S^F \right)^k, \quad (12)$$

where the power is applied entry-wise to each feature. The cumulants $\boldsymbol{\kappa}_S^{(k)}$ are then derived as follows (full formulae up to order 8 are provided in the SI XII):

$$\kappa_S^{(1)} = \bar{\xi}_S^F, \quad (13)$$

$$\kappa_S^{(2)} = \mu_S^{(2)}, \quad (14)$$

$$\kappa_S^{(3)} = \mu_S^{(3)}, \quad (15)$$

$$\kappa_S^{(4)} = \mu_S^{(4)} - 3(\mu_S^{(2)})^2, \quad (16)$$

$$\kappa_S^{(5)} = \mu_S^{(5)} - 10\mu_S^{(2)}\mu_S^{(3)}. \quad (17)$$

For numerical stability and to keep the scale of the descriptors comparable across orders, we use signed root cumulants:

$$\tilde{\kappa}_S^{(k)} = \text{sign}(\kappa_S^{(k)}) \cdot |\kappa_S^{(k)}|^{1/k}. \quad (18)$$

The cumulative structure-level descriptor up to order M is then a concatenation:

$$\phi_S^{(M)} = \left[\tilde{\kappa}_S^{(1)}, \tilde{\kappa}_S^{(2)}, \dots, \tilde{\kappa}_S^{(M)} \right]. \quad (19)$$

To determine the order at which these descriptors converge, i.e., when additional moments add negligible new statistics, we compute the reconstruction errors using the last-layer atomic features of PET-MAD on the MAD test set.

The reconstruction errors for cumulative structure-level descriptors (Fig. 8) show a hierarchical information flow, where higher-order moments fully sublimate lower-order ones. In contrast, lower-order descriptors cannot reconstruct higher ones, with errors scaling with order. This asymmetry is expected as the higher moments encode novel distributional aspects, such as skewness, beyond the mean and variance. This implies that structures with limited variability in the atomic environments, e.g., pristine crystals, lower orders may suffice in the global feature construction, but for most systems with high local variability, higher moments are needed to capture rare or asymmetric contributions. While the errors decrease progressively, they do not yet saturate by the eighth order: GFRE and LFRE for reconstructing the eighth order from the seventh are still above 0.3. This hints that more statistically meaningful structural inhomogeneities would be captured by going to even higher cumulants.

Applying eighth-order cumulative descriptors to cross-model analysis on the same MAD test dataset (SI XII Fig. S10) yields patterns similar to atomic-level features (Fig. 1) but with amplified dissimilarities. Overall, the errors are much higher (on average, the GFRE

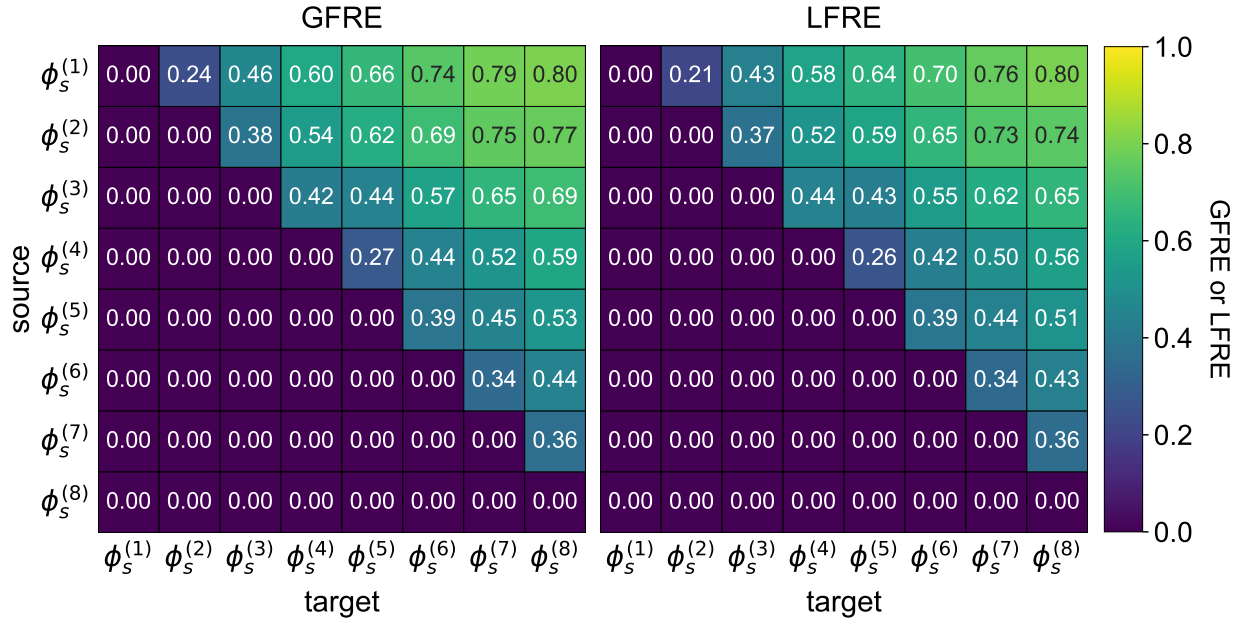


FIG. 8. The reconstruction errors of the progressive cumulative structure-level features, constructed as concatenations of central moments of last-layer features per atom. The features are derived from PET-MAD for the MAD test subset. $\phi_S^{(m)}$ denote cumulative descriptors up to order m . For the local feature reconstruction error (LFRE), we set the neighborhood size k to the larger feature dimension between the compared feature pairs.

is now 0.87, and LFRE is 0.83). This pattern suggests that the differences in the model latent features arising from the rare or asymmetric atomic-environment contributions is better captured by the higher cumulants. Practically, if the goal is to discriminate subtle model embeddings and emphasize rare motifs, inclusion of the higher cumulants is highly recommended.

To further illustrate the impact of higher-order statistics, we compare PCovR projections of structure-level descriptors built from mean-only features ($\tilde{\kappa}_S^{(1)}$) with those using full eighth-order cumulative cumulants ($\phi_S^{(8)}$) (Fig. 9). When only the mean atomic features are used (top row), the projections exhibit a loosely consistent motif, characterized by a linear cluster corresponding to a few of the subsets and then the remaining subsets dispersed around it. Even at this level, however, the exact shape and subset assignment around the projection motif vary across the different models. For the eighth-order cumulant descriptors (middle row), the linear cluster fragments disappear entirely for MACE-MP-0b3, PET-MAD, and DPA-3.1, and the overall point distributions become highly model-specific

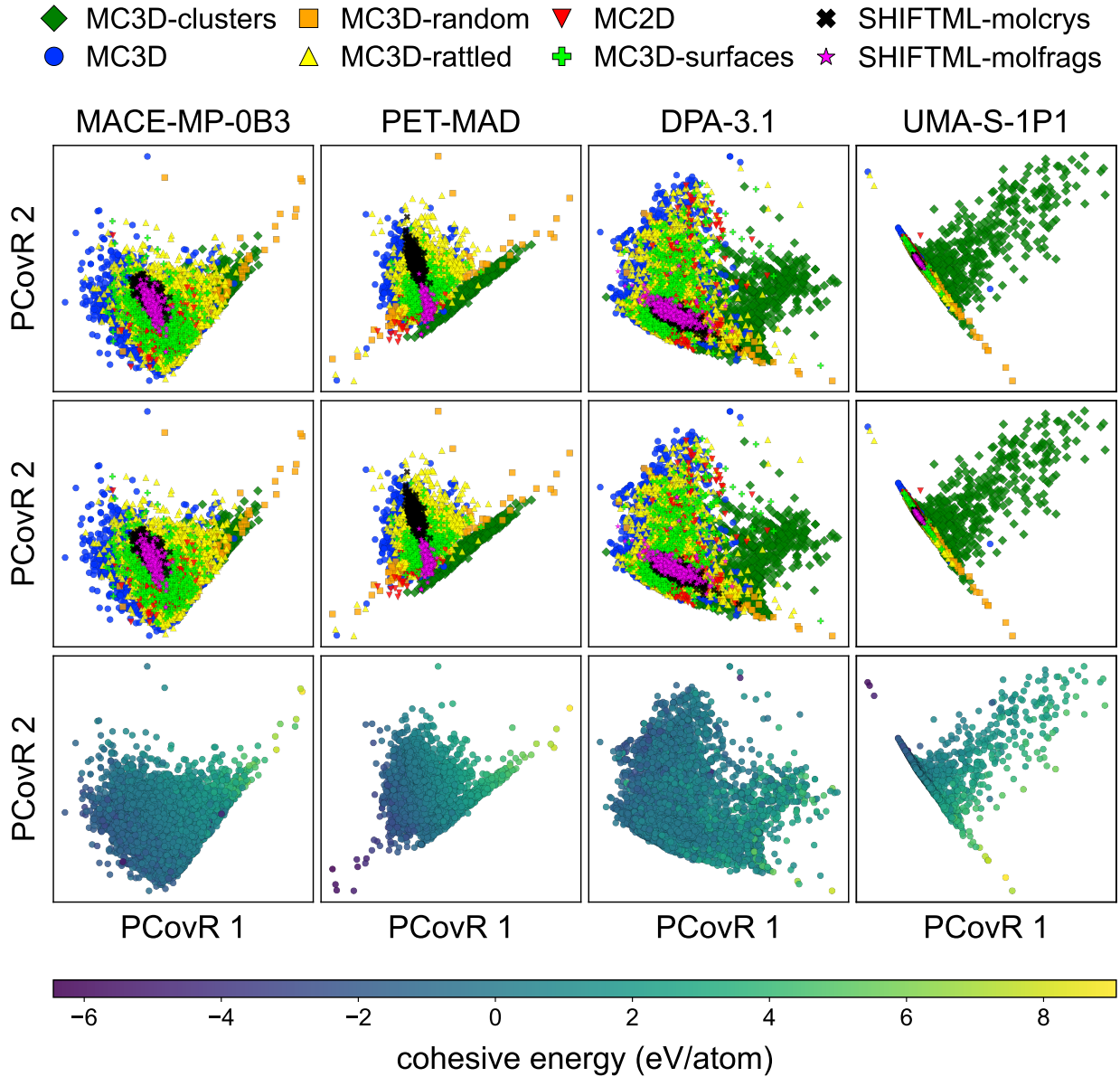


FIG. 9. The PCovR projections of structure-level descriptors for different uMLIPs on the MAD test subset. Top row: projections using mean atomic features ($\tilde{\kappa}_S^{(1)}$), colored by the different structural subsets of the MAD dataset. Middle row: projections using eighth-order cumulative cumulant features ($\phi_S^{(8)}$), again colored by respective structural subsets. Bottom row: same eighth-order cumulant features colored by the structural cohesive energy used as target in PCovR analysis.

with almost no cross-model alignment. Such vast differences are consistent with the higher values of the GFRE and LFRE observed between the uMLIPs in SI XII Fig. S10.

IV. CONCLUSIONS

The rapidly growing number of “universal” atomistic machine learning potentials and models, differing in architecture and training strategy but capable of achieving similar accuracies on benchmarks, raises questions of how the different models achieve their learning targets, especially in terms of their internal representations of the chemical systems. In this work, we have carried out systematic comparisons of the latent spaces of several universal ML models and their variants, using the feature reconstruction error metrics that quantitatively compare the “information content” of different sets of features. We see that the reconstruction errors are generally high between the latent features of different uMLIPs, revealing the presence of significant differences between the internal representations of the models despite their comparable accuracy. The local feature reconstruction errors are lower, which indicate the existence of nonlinear relations between the features of different models. They are nevertheless substantial, which suggests that different models choose to retain distinct structural and chemical information.

When comparing the variants of the same model architecture trained on different “universal” datasets, the trend becomes highly dependent on the adopted training strategy, with single-task and multi-head models exhibiting higher similarities than a model trained with the MoLE. We also note that the model variant corresponding to the large OMat24 dataset generally exhibits the smallest reconstruction errors compared to the other cases. This hints that a large, diverse dataset is not only beneficial for pre-training, but also encourages the learning of richer internal representations. A similar trend is observed when comparing the PET-MAD with PET-MAD-DOS, a model built from the same architecture and training set but targeting the energy-resolved electronic density of states, thereby yielding more information-rich features.

The role of training becomes apparent when considering the analysis of models fine-tuned on a more specific dataset. We observe that all fine-tuning strategies allow near-perfect reconstruction from and to the latent space of the original model. A model trained entirely from scratch on the small, domain-specific dataset achieves moderate (but larger than for fine-tuned models) reconstruction errors against those fine-tuned from a uMLIP, at least within the narrow portion of configuration space covered by the specific dataset.

The comparison between the backbone and last-layer features reveals that the backbone

layer contains relatively richer information, which retrospectively explains the success of using multiple heads for different prediction targets. In the particular case of PET-MAD, a rotationally unconstrained model, we further attribute the large information asymmetry to the fact that the deeper layers of PET would exhibit a non-invariant character that gets successively projected out as the model approaches the prediction of the scalar energy target. Lastly, we have extended the raw, atomic, local latent features of the uMLIPs to structural, global descriptors via higher-order cumulants. The higher cumulants fully subsume the lower-order statistics, which critically indicate that significant information becomes lost when using the averages of atomic features as structural descriptors, which is a common practice in the field.

Our results yield several practical insights for atomistic ML practitioners. In particular, one can apply the feature reconstruction error metrics to understand the information flow within a model architecture, for example, by quantifying how much generality is lost in the readout layers. One could also imagine using the GFRE and LFRE to guide the optimization of architectural hyperparameters to maximize the descriptive power of internal representations. In the context of fine-tuning, the changes in the latent features measured via the FREs can be linked to catastrophic forgetting and used to monitor the adjustments of the internal representations and prevent any significant loss of generalizability to out-of-distribution configurations. Given the hidden diversity of the uMLIP latent spaces uncovered in our study, we argue that predictive accuracy alone cannot sufficiently characterize atomistic ML models. Through the adoption of feature reconstruction error metrics, we establish a principled foundation for a more transparent, interpretable, and robust design of future atomistic ML models.

SOFTWARE AND DATA

The code and data required to reproduce the results of this work are available as a record [81] within the Materials Cloud [82] Archive (DOI: 10.24435/materialscloud:r5-vh). Model weights used in this work were obtained from their public repositories: `mace-foundations` (<https://github.com/ACEsuit/mace-foundations>), PET-MAD (<https://github.com/lab-cosmo/pet-mad>), DPA-3.1-3M (<https://www.aissquare.com/models/detail?name=DPA-3.1-3M&id=343&pageType=models>), and `fairchem` (<https://fair-chem.github.io>).

io/). Original datasets can be obtained from the respective cited sources.

ACKNOWLEDGMENTS

We thank A. Mazitov and F. Bigi for helpful discussions about the use of PET-MAD and its fine-tuning strategies. SoC, SaC, CM, DT, and MC acknowledge support from NCCR-MARVEL, funded by the Swiss National Science Foundation (SNSF) (grant number 205602). SaC and MC acknowledge support from a SNSF grant (project ID 200020_214879). DT and MC acknowledge support from a Sinergia grant of the SNSF (grant ID CRSII5_202296). WBH and MC acknowledges support from the European Research Council (ERC) under the research and innovation program (Grant Agreement No. 101001890-FIAMMA). This work was supported by grants from the Swiss National Supercomputing Centre (CSCS) under the projects s1243, s1219, lp26, and lp95.

- [1] Ryan Jacobs, Dane Morgan, Siamak Attarian, Jun Meng, Chen Shen, Zhenghao Wu, Clare Yijia Xie, Julia H. Yang, Nongnuch Artrith, Ben Blaiszik, Gerbrand Ceder, Kamal Choudhary, Gabor Csanyi, Ekin Dogus Cubuk, Bowen Deng, Ralf Drautz, Xiang Fu, Jonathan Godwin, Vasant Honavar, Olexandr Isayev, Anders Johansson, Boris Kozinsky, Stefano Martiniani, Shyue Ping Ong, Igor Poltavsky, KJ Schmidt, So Takamoto, Aidan P. Thompson, Julia Westermayr, and Brandon M. Wood, “A practical guide to machine learning interatomic potentials – status and future,” *Current Opinion in Solid State and Materials Science* **35**, 101214 (2025).
- [2] Jonathan Schmidt, Mário R. G. Marques, Silvana Botti, and Miguel A. L. Marques, “Recent advances and applications of machine learning in solid-state materials science,” *npj Computational Materials* **5**, 83 (2019).
- [3] Eric Qu and Aditi S. Krishnapriyan, “The importance of being scalable: Improving the speed and accuracy of neural network interatomic potentials across chemical domains,” in *Advances in Neural Information Processing Systems*, Vol. 37, edited by A. Globerson, L. Mackey, D. Belgrave, A. Fan, U. Paquet, J. Tomczak, and C. Zhang (Curran Associates, Inc., 2024) pp. 139030–139053.

[4] Chiheb Ben Mahmoud, Andrea Anelli, Gábor Csányi, and Michele Ceriotti, “Learning the electronic density of states in condensed matter,” *Phys. Rev. B* **102**, 235130 (2020).

[5] Wei Bin How, Sanggyu Chong, Federico Grasselli, Kevin K. Huguenin-Dumittan, and Michele Ceriotti, “Adaptive energy reference for machine-learning models of the electronic density of states,” *Phys. Rev. Mater.* **9**, 013802 (2025).

[6] K. T. Schütt, M. Gastegger, A. Tkatchenko, K. R. Müller, and R. J. Maurer, “Unifying machine learning and quantum chemistry with a deep neural network for molecular wavefunctions,” *Nature Communications* **10**, 5024 (2019).

[7] Divya Suman, Jigyasa Nigam, Sandra Saade, Paolo Pegolo, Hanna Türk, Xing Zhang, Garnet Kin-Lic Chan, and Michele Ceriotti, “Exploring the design space of machine learning models for quantum chemistry with a fully differentiable framework,” *Journal of Chemical Theory and Computation* **21**, 6505–6516 (2025).

[8] Duo Zhang, Anyang Peng, Chun Cai, Wentao Li, Yuanchang Zhou, Jinzhe Zeng, Mingyu Guo, Chengqian Zhang, Bowen Li, Hong Jiang, Tong Zhu, Weile Jia, Linfeng Zhang, and Han Wang, “A graph neural network for the era of large atomistic models,” (2025), arXiv:2506.01686 [physics.comp-ph].

[9] Brandon M. Wood, Misko Dzamba, Xiang Fu, Meng Gao, Muhammed Shuaibi, Luis Barroso-Luque, Kareem Abdelmaqsoud, Vahe Gharakhanyan, John R. Kitchin, Daniel S. Levine, Kyle Michel, Anuroop Sriram, Taco Cohen, Abhishek Das, Ammar Rizvi, Sushree Jagriti Sahoo, Zachary W. Ulissi, and C. Lawrence Zitnick, “Uma: A family of universal models for atoms,” (2025), arXiv:2506.23971 [cs.LG].

[10] Ilyes Batatia, Philipp Benner, Yuan Chiang, Alin M. Elena, Dávid P. Kovács, Janosh Riebesell, Xavier R. Advincula, Mark Asta, Matthew Avaylon, William J. Baldwin, Fabian Berger, Noam Bernstein, Arghya Bhowmik, Filippo Bigi, Samuel M. Blau, Vlad Cărare, Michele Ceriotti, Sanggyu Chong, James P. Darby, Sandip De, Flaviano Della Pia, Volker L. Deringer, Rokas Elijošius, Zakariya El-Machachi, Edvin Fako, Fabio Falcioni, Andrea C. Ferrari, John L. A. Gardner, Mikołaj J. Gawkowski, Annalena Genreith-Schriever, Janine George, Rhys E. A. Goodall, Jonas Grandel, Clare P. Grey, Petr Grigorev, Shuang Han, Will Handley, Hendrik H. Heenen, Kersti Hermansson, Cheuk Hin Ho, Stephan Hofmann, Christian Holm, Jad Jaafar, Konstantin S. Jakob, Hyunwook Jung, Venkat Kapil, Aaron D. Kaplan, Nima Karimitari, James R. Kermode, Panagiotis Kourtis, Namu Kroupa, Jolla Kullgren, Matthew C.

Kuner, Domantas Kuryla, Guoda Liepuoniute, Chen Lin, Johannes T. Margraf, Ioan-Bogdan Magdău, Angelos Michaelides, J. Harry Moore, Aakash A. Naik, Samuel P. Niblett, Sam Walton Norwood, Niamh O'Neill, Christoph Ortner, Kristin A. Persson, Karsten Reuter, Andrew S. Rosen, Louise A. M. Rosset, Lars L. Schaaf, Christoph Schran, Benjamin X. Shi, Eric Sivonxay, Tamás K. Stenczel, Christopher Sutton, Viktor Svahn, Thomas D. Swinburne, Jules Tilly, Cas van der Oord, Santiago Vargas, Eszter Varga-Umbrich, Tejs Vegge, Martin Vondrák, Yangshuai Wang, William C. Witt, Thomas Wolf, Fabian Zills, and Gábor Csányi, “A foundation model for atomistic materials chemistry,” *The Journal of Chemical Physics* **163**, 184110 (2025).

- [11] Ilyes Batatia, Chen Lin, Joseph Hart, Elliott Kasoar, Alin M. Elena, Sam Walton Norwood, Thomas Wolf, and Gábor Csányi, “Cross learning between electronic structure theories for unifying molecular, surface, and inorganic crystal foundation force fields,” (2025), arXiv:2510.25380 [physics.chem-ph].
- [12] Amil Merchant, Simon Batzner, Samuel S. Schoenholz, Muratahan Aykol, Gowoon Cheon, and Ekin Dogus Cubuk, “Scaling deep learning for materials discovery,” *Nature* **624**, 80–85 (2023).
- [13] Arslan Mazitov, Filippo Bigi, Matthias Kellner, Paolo Pegolo, Davide Tisi, Guillaume Fraux, Sergey Pozdnyakov, Philip Loche, and Michele Ceriotti, “Pet-mad as a lightweight universal interatomic potential for advanced materials modeling,” *Nature Communications* **16**, 10653 (2025).
- [14] Han Yang, Chenxi Hu, Yichi Zhou, Xixian Liu, Yu Shi, Jielan Li, Guanzhi Li, Zekun Chen, Shuizhou Chen, Claudio Zeni, Matthew Horton, Robert Pinsler, Andrew Fowler, Daniel Zügner, Tian Xie, Jake Smith, Lixin Sun, Qian Wang, Lingyu Kong, Chang Liu, Hongxia Hao, and Ziheng Lu, “Mattersim: A deep learning atomistic model across elements, temperatures and pressures,” (2024), arXiv:2405.04967 [cond-mat.mtrl-sci].
- [15] Anyang Peng, Chun Cai, Mingyu Guo, Duo Zhang, Chengqian Zhang, Wanrun Jiang, Yinan Wang, Antoine Loew, Chengkun Wu, Weinan E, Linfeng Zhang, and Han Wang, “Lambench: A benchmark for large atomistic models,” (2025), arXiv:2504.19578 [physics.comp-ph].
- [16] Bowen Deng, Peichen Zhong, KyuJung Jun, Janosh Riebesell, Kevin Han, Christopher J. Bartel, and Gerbrand Ceder, “Chgnet as a pretrained universal neural network potential for charge-informed atomistic modelling,” *Nature Machine Intelligence* **5**, 1031–1041 (2023).

- [17] Jonathan Schmidt, Tiago F.T. Cerqueira, Aldo H. Romero, Antoine Loew, Fabian Jäger, Hai-Chen Wang, Silvana Botti, and Miguel A.L. Marques, “Improving machine-learning models in materials science through large datasets,” *Materials Today Physics* **48**, 101560 (2024).
- [18] Arslan Mazitov, Sofia Chorna, Guillaume Fraux, Marnik Bercx, Giovanni Pizzi, Sandip De, and Michele Ceriotti, “Massive atomic diversity: a compact universal dataset for atomistic machine learning,” *Scientific Data* **12**, 1857 (2025).
- [19] Aaron D. Kaplan, Runze Liu, Ji Qi, Tsz Wai Ko, Bowen Deng, Janosh Riebesell, Gerbrand Ceder, Kristin A. Persson, and Shyue Ping Ong, “A foundational potential energy surface dataset for materials,” (2025), arXiv:2503.04070 [cond-mat.mtrl-sci].
- [20] Peter Eastman, Pavan Kumar Behara, David L. Dotson, Raimondas Galvelis, John E. Herr, Josh T. Horton, Yuezhi Mao, John D. Chodera, Benjamin P. Pritchard, Yuanqing Wang, Gianni De Fabritiis, and Thomas E. Markland, “Spice, a dataset of drug-like molecules and peptides for training machine learning potentials,” *Scientific Data* **10**, 11 (2023).
- [21] Lowik Chanussot, Abhishek Das, Siddharth Goyal, Thibaut Lavril, Muhammed Shuaibi, Morgane Riviere, Kevin Tran, Javier Heras-Domingo, Caleb Ho, Weihua Hu, Aini Palizhati, Anuroop Sriram, Brandon Wood, Junwoong Yoon, Devi Parikh, C. Lawrence Zitnick, and Zachary Ulissi, “Open catalyst 2020 (oc20) dataset and community challenges,” *ACS Catalysis* **11**, 6059–6072 (2021).
- [22] Anuroop Sriram, Sihoon Choi, Xiaohan Yu, Logan M. Brabson, Abhishek Das, Zachary Ulissi, Matt Uyttendaele, Andrew J. Medford, and David S. Sholl, “The open dac 2023 dataset and challenges for sorbent discovery in direct air capture,” (2023), arXiv:2311.00341 [cond-mat.mtrl-sci].
- [23] Luis Barroso-Luque, Muhammed Shuaibi, Xiang Fu, Brandon M. Wood, Misko Dzamba, Meng Gao, Ammar Rizvi, C. Lawrence Zitnick, and Zachary W. Ulissi, “Open materials 2024 (omat24) inorganic materials dataset and models,” (2024), arXiv:2410.12771 [cond-mat.mtrl-sci].
- [24] Vahe Gharakhanyan, Luis Barroso-Luque, Yi Yang, Muhammed Shuaibi, Kyle Michel, Daniel S. Levine, Misko Dzamba, Xiang Fu, Meng Gao, Xingyu Liu, Haoran Ni, Keian Noori, Brandon M. Wood, Matt Uyttendaele, Arman Boromand, C. Lawrence Zitnick, Noa Marom, Zachary W. Ulissi, and Anuroop Sriram, “Open molecular crystals 2025 (omc25) dataset and models,” (2025), arXiv:2508.02651 [physics.chem-ph].

[25] Daniel S. Levine, Muhammed Shuaibi, Evan Walter Clark Spotte-Smith, Michael G. Taylor, Muhammad R. Hasyim, Kyle Michel, Ilyes Batatia, Gábor Csányi, Misko Dzamba, Peter Eastman, Nathan C. Frey, Xiang Fu, Vahe Gharakhanyan, Aditi S. Krishnapriyan, Joshua A. Rackers, Sanjeev Raja, Ammar Rizvi, Andrew S. Rosen, Zachary Ulissi, Santiago Vargas, C. Lawrence Zitnick, Samuel M. Blau, and Brandon M. Wood, “The open molecules 2025 (omol25) dataset, evaluations, and models,” (2025), arXiv:2505.08762 [physics.chem-ph].

[26] Janosh Riebesell, Rhys E. A. Goodall, Philipp Benner, Yuan Chiang, Bowen Deng, Gerbrand Ceder, Mark Asta, Alpha A. Lee, Anubhav Jain, and Kristin A. Persson, “A framework to evaluate machine learning crystal stability predictions,” *Nature Machine Intelligence* **7**, 836–847 (2025).

[27] Anyang Peng, Chun Cai, Mingyu Guo, Duo Zhang, Chengqian Zhang, Wanrun Jiang, Yinan Wang, Antoine Loew, Chengkun Wu, Weinan E, Limfeng Zhang, and Han Wang, “Lambench: A benchmark for large atomistic models,” (2025), arXiv:2504.19578 [physics.comp-ph].

[28] Yuan Chiang, Tobias Kreiman, Christine Zhang, Matthew C. Kuner, Elizabeth Weaver, Ishan Amin, Hyunsoo Park, Yunsung Lim, Jihan Kim, Daryl Chrzan, Aron Walsh, Samuel M. Blau, Mark Asta, and Aditi S. Krishnapriyan, “Mlip arena: Advancing fairness and transparency in machine learning interatomic potentials via an open, accessible benchmark platform,” (2025), arXiv:2509.20630 [physics.chem-ph].

[29] Klara Bonneau, Jonas Lederer, Clark Templeton, David Rosenberger, Lorenzo Giambagli, Klaus-Robert Müller, and Cecilia Clementi, “Peering inside the black box by learning the relevance of many-body functions in neural network potentials,” *Nature Communications* **16**, 9898 (2025).

[30] Filippo Bigi, Sanggyu Chong, Michele Ceriotti, and Federico Grasselli, “A prediction rigidity formalism for low-cost uncertainties in trained neural networks,” *Machine Learning: Science and Technology* **5**, 045018 (2024).

[31] Albert Zhu, Simon Batzner, Albert Musaelian, and Boris Kozinsky, “Fast uncertainty estimates in deep learning interatomic potentials,” *The Journal of Chemical Physics* **158**, 164111 (2023).

[32] Luis Itza Vazquez-Salazar, Eric D. Boittier, and Markus Meuwly, “Uncertainty quantification for predictions of atomistic neural networks,” *Chem. Sci.* **13**, 13068–13084 (2022).

- [33] Maksim Kulichenko, Kipton Barros, Nicholas Lubbers, Ying Wai Li, Richard Messerly, Sergei Tretiak, Justin S. Smith, and Benjamin Nebgen, “Uncertainty-driven dynamics for active learning of interatomic potentials,” *Nature Computational Science* **3**, 230–239 (2023).
- [34] Jon Paul Janet, Chenru Duan, Tzuhsing Yang, Aditya Nandy, and Heather J. Kulik, “A quantitative uncertainty metric controls error in neural network-driven chemical discovery,” *Chem. Sci.* **10**, 7913–7922 (2019).
- [35] Christian W. Feldmann, Jochen Sieg, and Miriam Mathea, “Analysis of uncertainty of neural fingerprint-based models,” *Faraday Discuss.* **256**, 551–567 (2025).
- [36] Luis Itza Vazquez-Salazar, Silvan Käser, and Markus Meuwly, “Outlier-detection for reactive machine learned potential energy surfaces,” *npj Computational Materials* **11**, 33 (2025).
- [37] Daniel Schwalbe-Koda, Sébastien Hamel, Babak Sadigh, Fei Zhou, and Vincenzo Lordi, “Model-free estimation of completeness, uncertainties, and outliers in atomistic machine learning using information theory,” *Nature Communications* **16** (2025), 10.1038/s41467-025-59232-0.
- [38] Yu Xie, Jonathan Vandermause, Lixin Sun, Andrea Cepellotti, and Boris Kozinsky, “Bayesian force fields from active learning for simulation of inter-dimensional transformation of stanene,” *npj Computational Materials* **7**, 40 (2021).
- [39] Jonathan Vandermause, Steven B. Torrisi, Simon Batzner, Yu Xie, Lixin Sun, Alexie M. Kolpak, and Boris Kozinsky, “On-the-fly active learning of interpretable bayesian force fields for atomistic rare events,” *npj Computational Materials* **6**, 20 (2020).
- [40] M. Kulichenko, B. Nebgen, N. Lubbers, J. S. Smith, K. Barros, A. E. A. Allen, A. Habib, E. Shinkle, N. Fedik, Y. W. Li, R. A. Messerly, and S. Tretiak, “Data generation for machine learning interatomic potentials and beyond,” *Chemical Reviews* **124**, 13681–13714 (2024).
- [41] Joanna Zou and Youssef Marzouk, “Data curation for machine learning interatomic potentials by determinantal point processes,” in *Proceedings of the International Conference on Learning Representations (ICLR)* (2025).
- [42] Aldo Glielmo, Claudio Zeni, Bingqing Cheng, Gábor Csányi, and Alessandro Laio, “Ranking the information content of distance measures,” *PNAS Nexus* **1**, pgac039 (2022).
- [43] Sandip De, Felix Musil, Teresa Ingram, Carsten Baldauf, and Michele Ceriotti, “Mapping and classifying molecules from a high-throughput structural database,” *Journal of Cheminformatics* **9**, 6 (2017).

[44] Christopher J. Bartel, Amalie Trewartha, Qi Wang, Alexander Dunn, Anubhav Jain, and Gerbrand Ceder, “A critical examination of compound stability predictions from machine-learned formation energies,” *npj Computational Materials* **6**, 97 (2020).

[45] Sathya Edamadaka, Soojung Yang, Ju Li, and Rafael Gómez-Bombarelli, “Universally converging representations of matter across scientific foundation models,” (2025), arXiv:2512.03750 [cs.LG].

[46] Zhenzhu Li and Aron Walsh, “Platonic representation of foundation machine learning interatomic potentials,” (2025), arXiv:2512.05349 [cond-mat.mtrl-sci].

[47] Alexander Goscinski, Guillaume Fraux, Giulio Imbalzano, and Michele Ceriotti, “The role of feature space in atomistic learning,” *Machine Learning: Science and Technology* **2**, 025028 (2021).

[48] Wei Bin How, Pol Febrer, Sanggyu Chong, Arslan Mazitov, Filippo Bigi, Matthias Kellner, Sergey Pozdnyakov, and Michele Ceriotti, “A universal machine learning model for the electronic density of states,” (2025), arXiv:2508.17418 [physics.chem-ph].

[49] Sergey Pozdnyakov and Michele Ceriotti, “Smooth, exact rotational symmetrization for deep learning on point clouds,” in *Advances in Neural Information Processing Systems (NeurIPS 2023)* (2023).

[50] Jinzhe Zeng, Duo Zhang, Anyang Peng, Xiangyu Zhang, Sensen He, Yan Wang, Xinzijian Liu, Hangrui Bi, Yifan Li, Chun Cai, Chengqian Zhang, Yiming Du, Jia-Xin Zhu, Pinghui Mo, Zhengtao Huang, Qiyu Zeng, Shaochen Shi, Xuejian Qin, Zhaoxi Yu, Chenxing Luo, Ye Ding, Yun-Pei Liu, Ruosong Shi, Zhenyu Wang, Sigbjørn Løland Bore, Junhan Chang, Zhe Deng, Zhaohan Ding, Siyuan Han, Wanrun Jiang, Guolin Ke, Zhaoqing Liu, Denghui Lu, Koki Muraoka, Hananeh Oliaei, Anurag Kumar Singh, Haohui Que, Weihong Xu, Zhangmancang Xu, Yong-Bin Zhuang, Jiayu Dai, Timothy J. Giese, Weile Jia, Ben Xu, Darrin M. York, Linfeng Zhang, and Han Wang, “DeePMD-kit v3: A Multiple-Backend Framework for Machine Learning Potentials,” *J. Chem. Theory Comput.* **21**, 4375–4385 (2025).

[51] Xiang Fu, Brandon M Wood, Luis Barroso-Luque, Daniel S. Levine, Meng Gao, Misko Dzamba, and C. Lawrence Zitnick, “Learning smooth and expressive interatomic potentials for physical property prediction,” in *Proceedings of the 42nd International Conference on Machine Learning*, Proceedings of Machine Learning Research, Vol. 267, edited by Aarti Singh, Maryam Fazel, Daniel Hsu, Simon Lacoste-Julien, Felix Berkenkamp, Tegan Maharaj,

Kiri Wagstaff, and Jerry Zhu (PMLR, 2025) pp. 17875–17893.

[52] Alexander Goscinski, Victor Paul Principe, Guillaume Fraux, Sergei Kliavinek, Benjamin Aaron Helfrecht, Philip Loche, Michele Ceriotti, and Rose Kathleen Cersonsky, “scikit-matter: A suite of generalisable machine learning methods born out of chemistry and materials science,” *Open Research Europe* **3**, 81 (2023).

[53] Sijmen de Jong and Henk A.L. Kiers, “Principal covariates regression: Part i. theory,” *Chemometrics and Intelligent Laboratory Systems* **14**, 155–164 (1992), proceedings of the 2nd Scandinavian Symposium on Chemometrics.

[54] Rose K Cersonsky, Benjamin A Helfrecht, Edgar A Engel, Sergei Kliavinek, and Michele Ceriotti, “Improving sample and feature selection with principal covariates regression,” *Machine Learning: Science and Technology* **2**, 035038 (2021).

[55] Rich Caruana, “Multitask learning,” *Machine Learning* **28**, 41–75 (1997).

[56] Sebastian Ruder, “An overview of multi-task learning in deep neural networks,” (2017), arXiv:1706.05098 [cs.LG].

[57] Robert A. Jacobs, Michael I. Jordan, Steven J. Nowlan, and Geoffrey E. Hinton, “Adaptive mixtures of local experts,” *Neural Computation* **3**, 79–87 (1991).

[58] Carlos Riquelme, Joan Puigcerver, Basil Mustafa, Maxim Neumann, Rodolphe Jenatton, André Susano Pinto, Daniel Keysers, and Neil Houlsby, “Scaling vision with sparse mixture of experts,” in *Advances in Neural Information Processing Systems*, Vol. 34 (2021) pp. 8583–8595.

[59] Noam Shazeer, Azalia Mirhoseini, Krzysztof Maziarz, Andy Davis, Quoc V. Le, Geoffrey Hinton, and Jeff Dean, “Outrageously large neural networks: The sparsely-gated mixture-of-experts layer,” in *Proceedings of the International Conference on Learning Representations (ICLR)* (2017).

[60] Jp P Perdew, K Burke, and M Ernzerhof, “Generalized Gradient Approximation made simple,” *Phys. Rev. Lett. Phys. Rev. Lett. (USA)*, **77**, 3865 (1996).

[61] James W. Furness, Aaron D. Kaplan, Jinliang Ning, John P. Perdew, and Jianwei Sun, “Accurate and numerically efficient r2scan meta-generalized gradient approximation,” *The Journal of Physical Chemistry Letters* **11**, 8208–8215 (2020).

[62] Yury Lysogorskiy, Anton Bochkarev, and Ralf Drautz, “Graph atomic cluster expansion for foundational machine learning interatomic potentials,” (2025), arXiv:2508.17936 [cond-

mat.mtrl-sci].

- [63] Benjamin Rhodes, Sander Vandenhaute, Vaidotas Šimkus, James Gin, Jonathan Godwin, Tim Duignan, and Mark Neumann, “Orb-v3: atomistic simulation at scale,” (2025), arXiv:2504.06231 [cond-mat.mtrl-sci].
- [64] Dávid Péter Kovács, J. Harry Moore, Nicholas J. Browning, Ilyes Batatia, Joshua T. Horton, Yixuan Pu, Venkat Kapil, William C. Witt, Ioan-Bogdan Magdău, Daniel J. Cole, and Gábor Csányi, “Mace-off: Short-range transferable machine learning force fields for organic molecules,” *Journal of the American Chemical Society* **147**, 17598–17611 (2025).
- [65] Laboratory of Computational Science and Modeling (COSMO), EPFL, “UPET: Universal interatomic potentials for advanced materials modeling,” <https://github.com/lab-cosmo/upet> (2026), online; accessed Jan. 2026.
- [66] Bowen Deng, Yunyeong Choi, Peichen Zhong, Janosh Riebesell, Shashwat Anand, Zhuohan Li, KyuJung Jun, Kristin A. Persson, and Gerbrand Ceder, “Overcoming systematic softening in universal machine learning interatomic potentials by fine-tuning,” (2024), arXiv:2405.07105 [cond-mat.mtrl-sci].
- [67] Mariia Radova, Wojciech G. Stark, Connor S. Allen, Reinhard J. Maurer, and Albert P. Bartók, “Fine-tuning foundation models of materials interatomic potentials with frozen transfer learning,” *npj Computational Materials* **11**, 237 (2025).
- [68] Harveen Kaur, Flaviano Della Pia, Ilyes Batatia, Xavier R. Advincula, Benjamin X. Shi, Jinggang Lan, Gábor Csányi, Angelos Michaelides, and Venkat Kapil, “Data-efficient fine-tuning of foundational models for first-principles quality sublimation enthalpies,” *Faraday Discuss.* **256**, 120–138 (2025).
- [69] Zengcai Liu, Wujun Fu, E. Andrew Payzant, Xiang Yu, Zili Wu, Nancy J. Dudney, Jim Kiggans, Kunlun Hong, Adam J. Rondinone, and Chengdu Liang, “Anomalous High Ionic Conductivity of Nanoporous beta-Li₃ PS₄,” *J. Am. Chem. Soc.* **135**, 975–978 (2013).
- [70] Natascia L. Fragapane and Volker L. Deringer, “Li-p-s electrolyte materials as a benchmark for machine-learned interatomic potentials,” (2025), arXiv:2511.16569 [cond-mat.mtrl-sci].
- [71] Atsutaka Kato, Mari Yamamoto, Futoshi Utsuno, Hiroyuki Higuchi, and Masanari Takahashi, “Lithium-ion-conductive sulfide polymer electrolyte with disulfide bond-linked PS4 tetrahedra for all-solid-state batteries,” *Commun Mater* **2**, 112 (2021).

[72] Arumugam Manthiram, Xingwen Yu, and Shaofei Wang, “Lithium battery chemistries enabled by solid-state electrolytes,” *Nat Rev Mater* **2**, 16103 (2017).

[73] Davide Tisi, Federico Grasselli, Lorenzo Gigli, and Michele Ceriotti, “Thermal conductivity of Li₃PS₄ solid electrolytes with *ab initio* accuracy,” *Phys. Rev. Materials* **8**, 065403 (2024).

[74] Lorenzo Gigli, Davide Tisi, Federico Grasselli, and Michele Ceriotti, “Mechanism of Charge Transport in Lithium Thiophosphate,” *Chem. Mater.* **36**, 1482–1496 (2024).

[75] Filippo Bigi, Joseph W. Abbott, Philip Loche, Arslan Mazitov, Davide Tisi, Marcel F. Langer, Alexander Goscinski, Paolo Pegolo, Sanggyu Chong, Rohit Goswami, Sofia Chorna, Matthias Kellner, Michele Ceriotti, and Guillaume Fraux, “Metatensor and metatomic: Foundational libraries for interoperable atomistic machine learning,” (2025).

[76] Hanna Türk, Davide Tisi, and Michele Ceriotti, “Reconstructions and dynamics of β -lithium thiophosphate surfaces,” *PRX Energy* **4**, 033010 (2025).

[77] Gareth A Tribello, Michele Ceriotti, and Michele Parrinello, “Using sketch-map coordinates to analyze and bias molecular dynamics simulations.” *Proc. Natl. Acad. Sci. USA* **109**, 5196–201 (2012).

[78] Olexandr Isayev, Denis Fourches, Eugene N. Muratov, Corey Oses, Kevin Rasch, Alexander Tropsha, and Stefano Curtarolo, “Materials cartography: Representing and mining materials space using structural and electronic fingerprints,” *Chemistry of Materials* **27**, 735–743 (2015).

[79] Haoyue Guo, Qian Wang, Alexander Urban, and Nongnuch Artrith, “Artificial intelligence-aided mapping of the structure–composition–conductivity relationships of glass–ceramic lithium thiophosphate electrolytes,” *Chemistry of Materials* **34**, 6702–6712 (2022).

[80] Bingqing Cheng, Ryan-Rhys Griffiths, Simon Wengert, Christian Kunkel, Tamas Stenczel, Bonan Zhu, Volker L. Deringer, Noam Bernstein, Johannes T. Margraf, Karsten Reuter, and Gabor Csanyi, “Mapping materials and molecules,” *Accounts of Chemical Research* **53**, 1981–1991 (2020).

[81] Sofia Chorna, Davide Tisi, Cesare Malosso, Wei Bin How, and Michele Ceriotti, “Comparing the latent features of universal machine-learning interatomic potentials,” <https://doi.org/10.24435/materialscloud:gb-5z> (2025).

[82] Leopold Talirz, Snehal Kumbhar, Elsa Passaro, Aliaksandr V. Yakutovich, Valeria Granata, Fernando Gargiulo, Marco Borelli, Martin Uhrin, Sebastiaan P. Huber, Spyros Zoupanos, Carl S. Adorf, Casper Welzel Andersen, Ole Schütt, Carlo A. Pignedoli, Daniele Passerone,

Joost VandeVondele, Thomas C. Schulthess, Berend Smit, Giovanni Pizzi, and Nicola Marzari,
“Materials cloud, a platform for open computational science,” *Scientific Data* **7** (2020),
10.1038/s41597-020-00637-5.

Supplementary Information

V. FEATURE SPACE COMPARISON METRICS

To aid the reader's understanding of the the difference between the global feature reconstruction error (GFRE) and the local feature reconstruction error (LFRE) introduced in Sec. II A, we present a minimal illustrative example in Fig. S1.

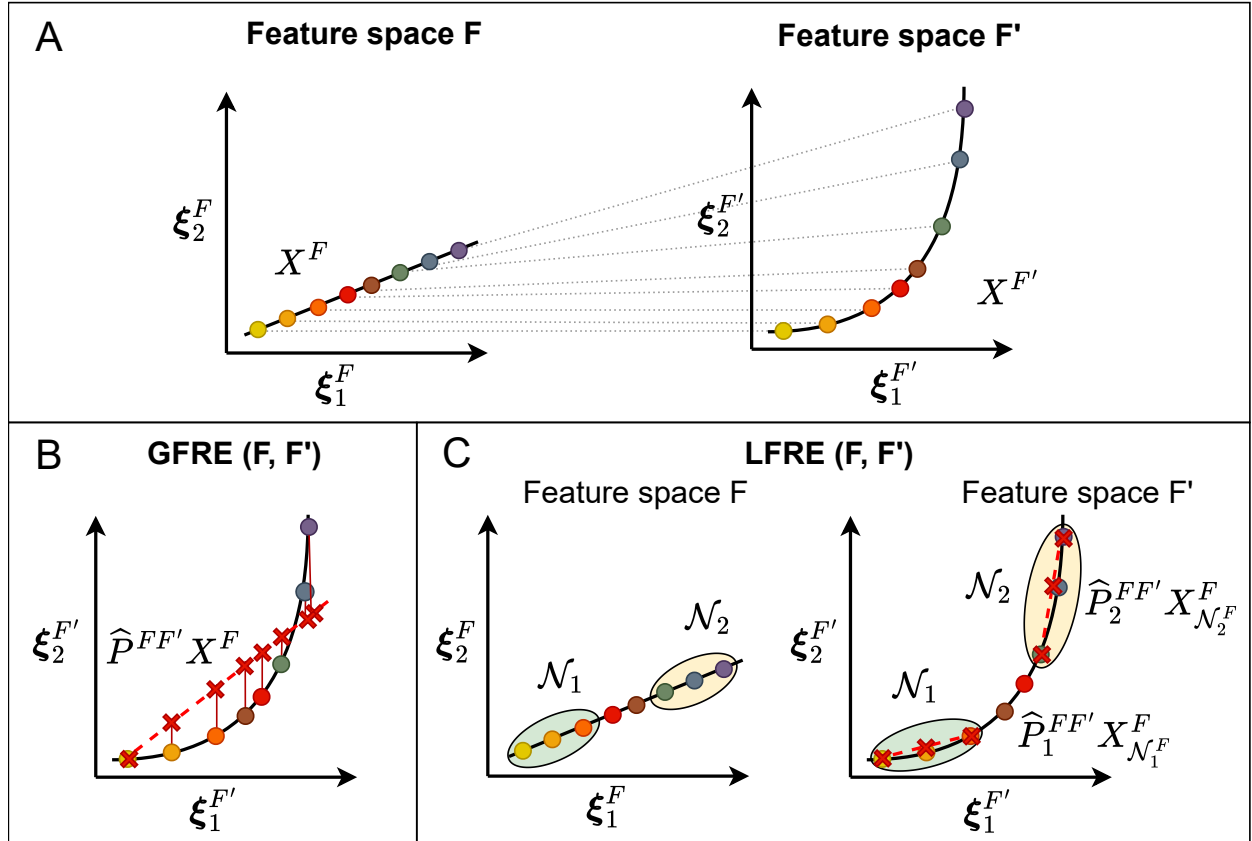


FIG. S1. A schematic overview of the global (GFRE) and local (LFRE) feature reconstruction errors. (A) shows a one-dimensional manifold of atomic environments embedded into two two-dimensional feature spaces, F and F' , related by a nonlinear transformation. (B) illustrates $\text{GFRE}(F, F')$, where a single global linear mapping $\hat{P}^{FF'}$ is applied to reconstruct F' from F . The dashed red line indicates the globally optimal linear fit $\hat{P}^{FF'} X^F$. (C) shows $\text{LFRE}(F, F')$: for each atomic environment i , a separate local linear mapping $\hat{P}_{(i)}^{FF'}$ is fitted to its k nearest neighbors \mathcal{N}_i in feature space F .

VI. LATENT FEATURE COMPARISON BETWEEN UMLIPS ON ALEXANDRIA DATASET

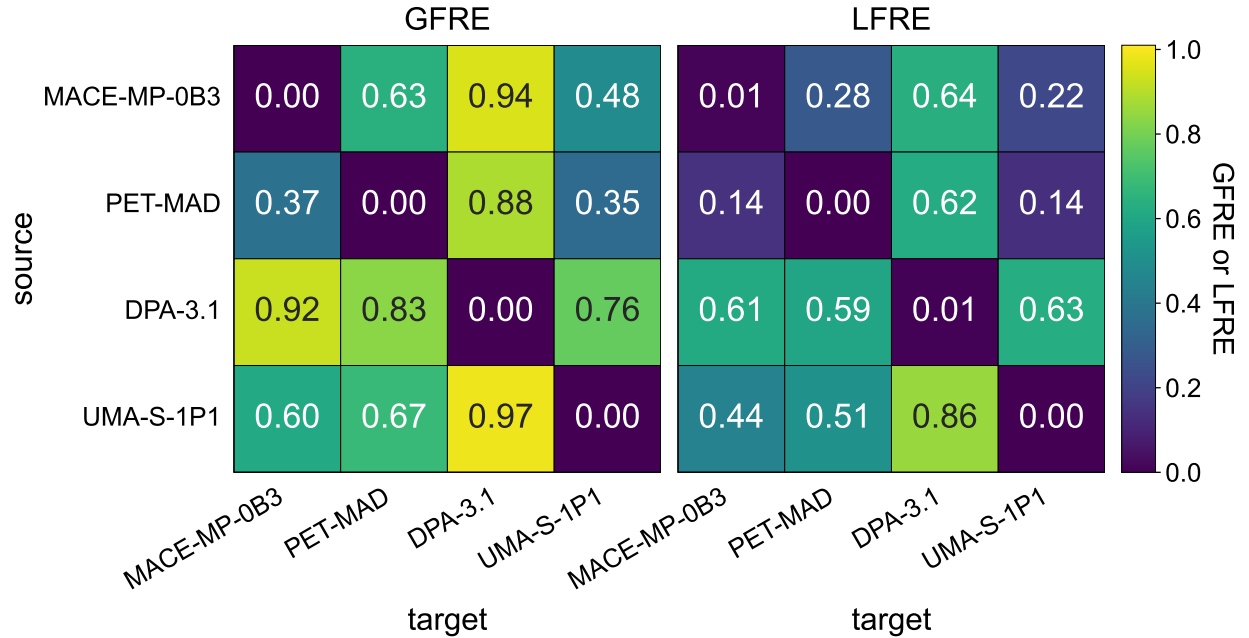


FIG. S2. The reconstruction errors for atomic last-layer latent features of MACE-MP-03b, PET-MAD, DPA-3.1, and UMA-S-1P1, computed for the atomic environments sampled from the sAlex dataset.

To ensure independence from training distributions and mitigate potential biases, we evaluate reconstruction errors on the subsampled Alexandria dataset (sAlex) [17, 23], which contains a broad coverage of inorganic materials across three-, two-, and one-dimensional periodic structures. We first randomly select 20,000 structures from the validation split, then filter to exclude the single-atom structures and structures with no interatomic distances below 6 Å (incompatible with UMA-S-1P1), and those containing actinide elements (as atomic numbers 89–94 are not supported by MACE-MP-0b3), yielding 169,836 atomic environments from 16,306 structures. From these, 1000 atomic environments are randomly sampled to comprise $\mathcal{D}_{\text{test}}$, and all remaining environments are used as $\mathcal{D}_{\text{train}}$ to obtain the regression weights $\hat{P}_{FF'}$.

Similarly to the results on MAD test (see Fig. 1 in the main text), PET-MAD reconstructs other models' feature spaces with the lowest GFRE and LFRE (on average 0.53 and 0.3, respectively), as shown in Fig. S2. The high incoming and outgoing errors for DPA-3.1

suggest that its latent space is particularly orthogonal to other models.

VII. COMPARING BACKBONE FEATURES OF UMLIPS

The lower reconstruction errors for backbone features (average off-diagonal GFRE 0.54 vs 0.66 for last-layer, LFRE 0.30 vs 0.37) indicate that representations immediately after message-passing are more consistent and linearly reconstructable.

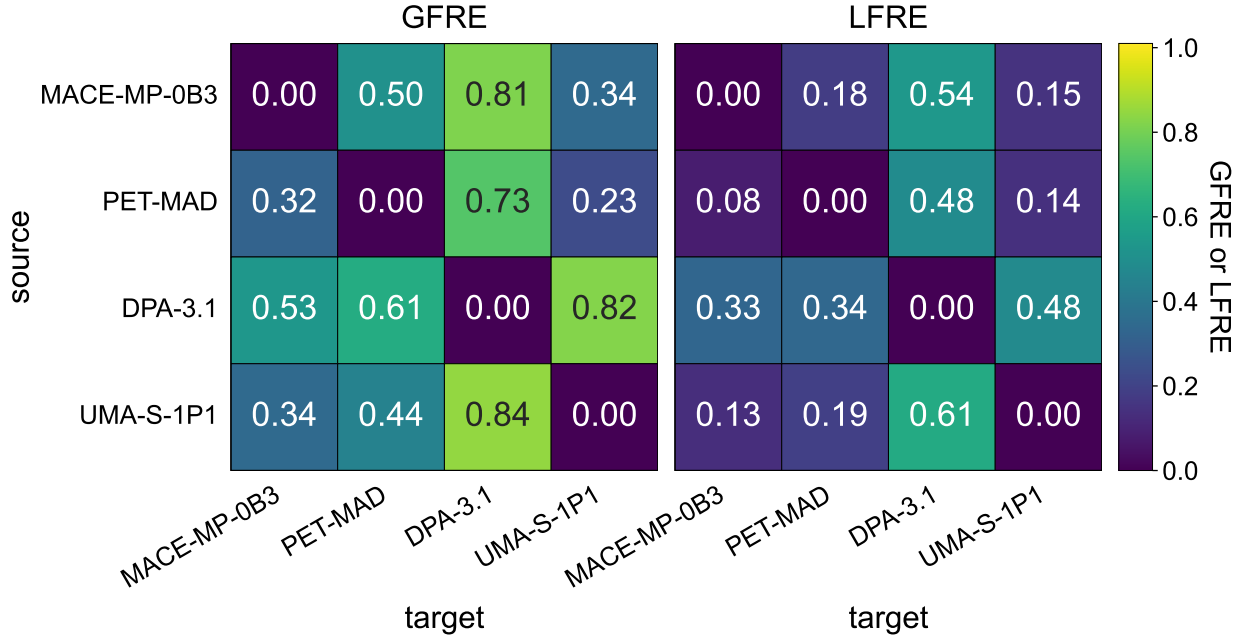


FIG. S3. The reconstruction errors for atomic backbone features computed across MACE-MP-0b3, PET-MAD, DPA-3.1, and UMA-S-1P1, evaluated on the MAD test subset. Compared to last-layer features (Fig. 1), backbone representations exhibit consistently lower cross-model errors.

VIII. COMPARING MODEL VARIANTS

A. Multi-task handling

1. DPA-3.1

DPA-3.1 incorporates a multi-task framework with a shared backbone network conditioned on dataset identifiers via one-hot encoding [8]. We compare its branches correspond-

ing to OMat24, MPtrj, OC20, ODAC, and SPICE [16, 20–23]. As shown in Fig. S4, the latent spaces of these branches are remarkably consistent despite the extreme diversity of the underlying data. LFRE remains particularly low (with the maximum of 0.14), indicating highly similar local neighborhoods across branches. This suggests that this multi-task design with full backbone sharing enforces highly similar latent representations across branches.

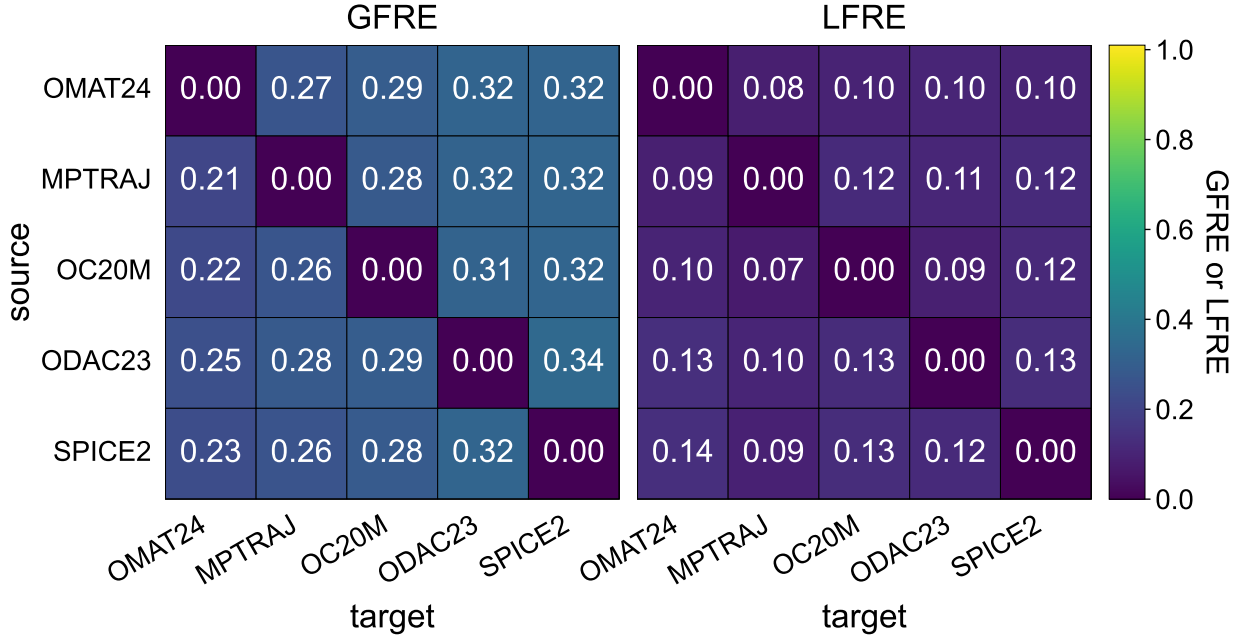


FIG. S4. Reconstruction errors among DPA-3.1 branches trained on OMat24, MPtrj, OC20, ODAC, and SPICE.

2. Universal PET checkpoints

Here, we evaluate the feature reconstruction errors across single-task PET universal models trained on different datasets. Table S1 summarizes the characteristics of the five PET variants analyzed, including model size and training protocol. All models were obtained from the public UPET repository [65]. From Fig. S5, MAD and OAM checkpoints are the most challenging to reconstruct with global linear approximation. OMat24 pretrained models (OMAD, OMAT, and OMATPES) show slightly lower reconstruction, sharing the same latent space foundation from the pre-training.

TABLE S1. Overview of PET model variants used in the reconstruction error analysis. All “O”-prefixed models are pre-trained on OMat24 before training on the target dataset. sAlex stands for the subsampled Alexandria dataset (sAlexandria) [17, 23].

Model	Pre-training	Target Dataset	DFT Level	Size
PET-MAD	—	MAD	PBESol	S
PET-OAM	OMat24	sAlexandria + MPtrj	PBE	L
PET-OMAD	OMat24	MAD	PBESol	L
PET-OMAT	OMat24	OMat24	PBE	L
PET-OMATPES	OMat24	MatPES	r2SCAN	L

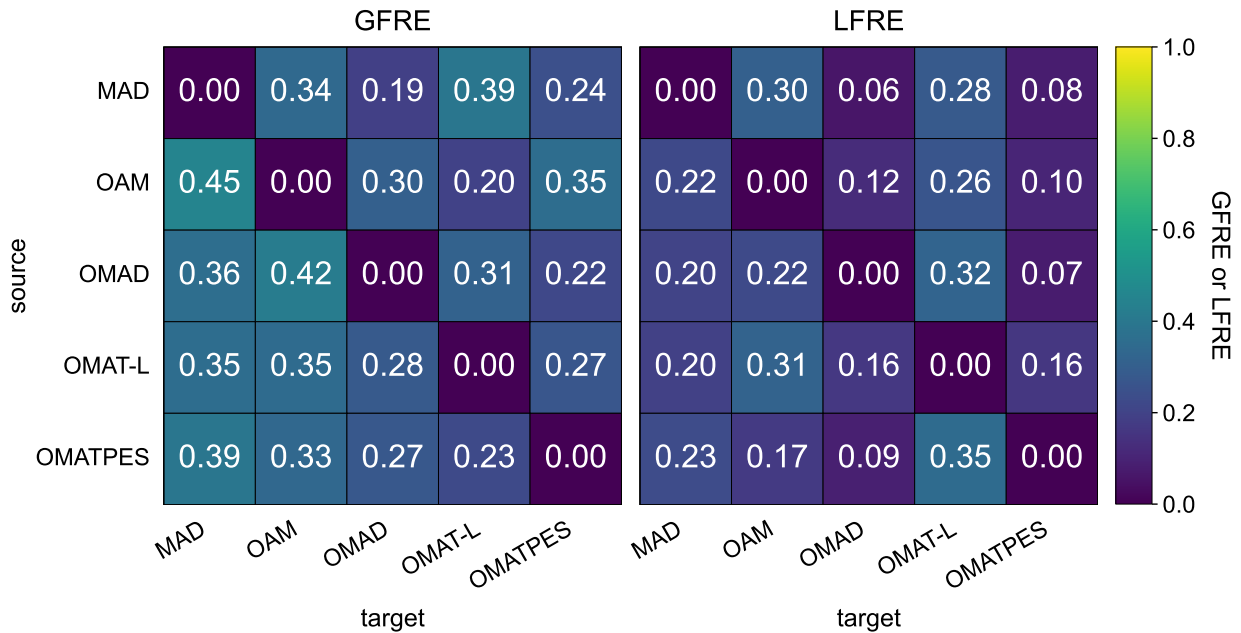


FIG. S5. Reconstruction errors among PET variants trained on MAD, OAM, OMAT, and OMAT-PES on the MAD test set [16, 18, 19, 23].

B. Dataset domain

We further probe the effect of training dataset domain by comparing medium-sized models, MACE-MP-0b3 [10] trained on MPtrj [16], a materials-focused dataset, and MACE-OFF23 [64] trained on SPICE [20], an organics-focused dataset.

Reconstruction errors have been computed for only the organic structures found within the MAD test set. From Table S2, MACE-MP-0b3 can reconstruct the organic-trained

model almost perfectly (GFRE = 0.02). In the reverse direction, the MACE-OFF23 fails to reconstruct the MACE-MP-0b3 features globally (GFRE = 0.36), despite near-perfect local feature reconstruction (LFRE = 0.04). This is explained by the fact that MACE-MP-0b3 was trained on a vastly more diverse dataset, and has learned a richer global mapping that MACE-OFF23 simply cannot replicate due to a significantly smaller dataset scope.

TABLE S2. GFRE and LFRE comparison between MACE-MP-03b and MACE-OFF23 evaluated on the organic structures of the MAD test set.

Reconstruction direction (source → target)	GFRE	LFRE
MP-03b → OFF23	0.02	0.06
OFF23 → MP-03b	0.36	0.04

C. Model sizes

1. MACE-MP-0a and MACE-OFF23

In this section, we examine how well the MACE models of different sizes (small, medium, large) can reconstruct the last-layer features of one another. In Fig. S6, the upper triangle shows results for the MPtrj-trained MACE-MP-0a evaluated on the MAD test subset, and the lower triangle shows the results for MACE-OFF23 [64] evaluated on the organic structures found in the MAD test subset.

Notably, MACE-MP-0a checkpoints reconstruct each other almost perfectly, regardless of the model size. For MACE-OFF23, error rises when a small or medium model tries to reconstruct the large one (GFRE is 0.48, LFRE is 0.31 on average between them), meaning the larger model contains expressive capacity that smaller models cannot fully replicate. These distinct trends could stem from the differences in the hyperparameters or training protocol between MACE-MP series and MACE-OFF, and/or the differences in the scope of the training datasets.

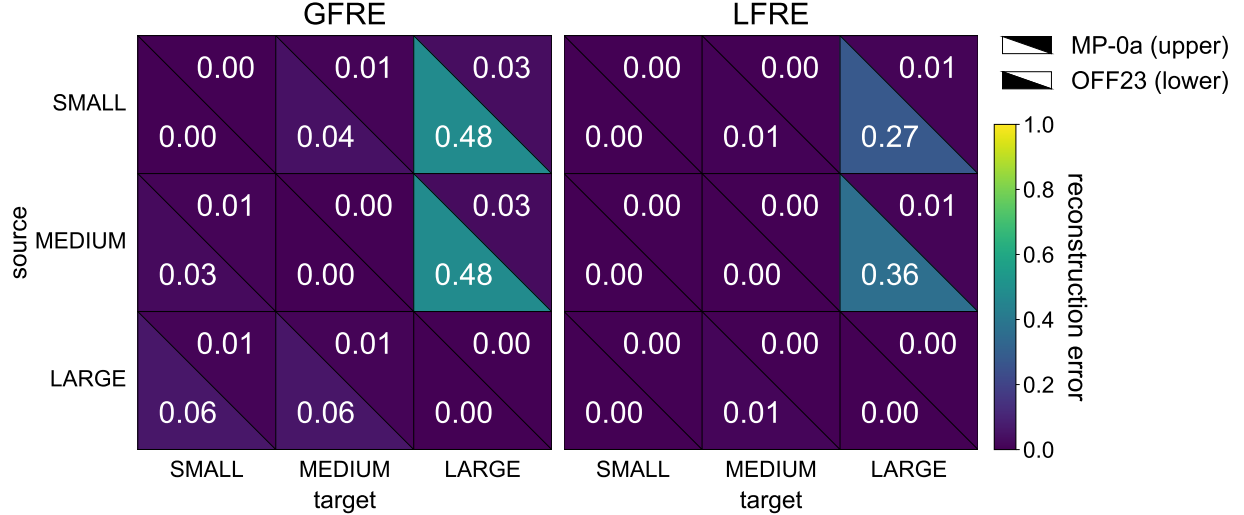


FIG. S6. GFRE (left) and LFRE (right) among MACE checkpoints of different sizes (small, medium, large) on the MAD test dataset. Upper triangles correspond to MACE-MP-0a (materials); lower to MACE-OFF23 (organics).

2. PET-OMAT

In addition to MACE variants, we also compare the PET-OMAT checkpoints [65] of different sizes. The model sizes depend on the combination of the number of GNN layers (N_{gnn}), the number of transformer layers (N_{tl}), the neural network width (d_{pet}), and the cutoff radius (r_{cut}) (see Table S3).

TABLE S3. PET-OMAT model hyperparameters.

Model Size	d_{pet}	N_{gnn}	N_{tl}	r_{cut} (Å)
XS	128	2	1	4.0
S	256	3	1	4.5
M	384	3	2	4.5
L	512	4	2	4.5

From the error heat maps (see Fig. S7), the models seem to share a common backbone in the latent space: smaller models (XS, S) can capture the main latent feature manifold of larger models (M, L) with reasonable accuracy. Local reconstruction errors are higher and have stronger asymmetry, which indicates that local feature neighborhoods are progressively better reconstructed as the model size increases. We argue that the M model provides a

favorable tradeoff, achieving low errors when reconstructing the L model, and can thus serve as an effective pre-training base for fine-tuning while remaining computationally efficient.

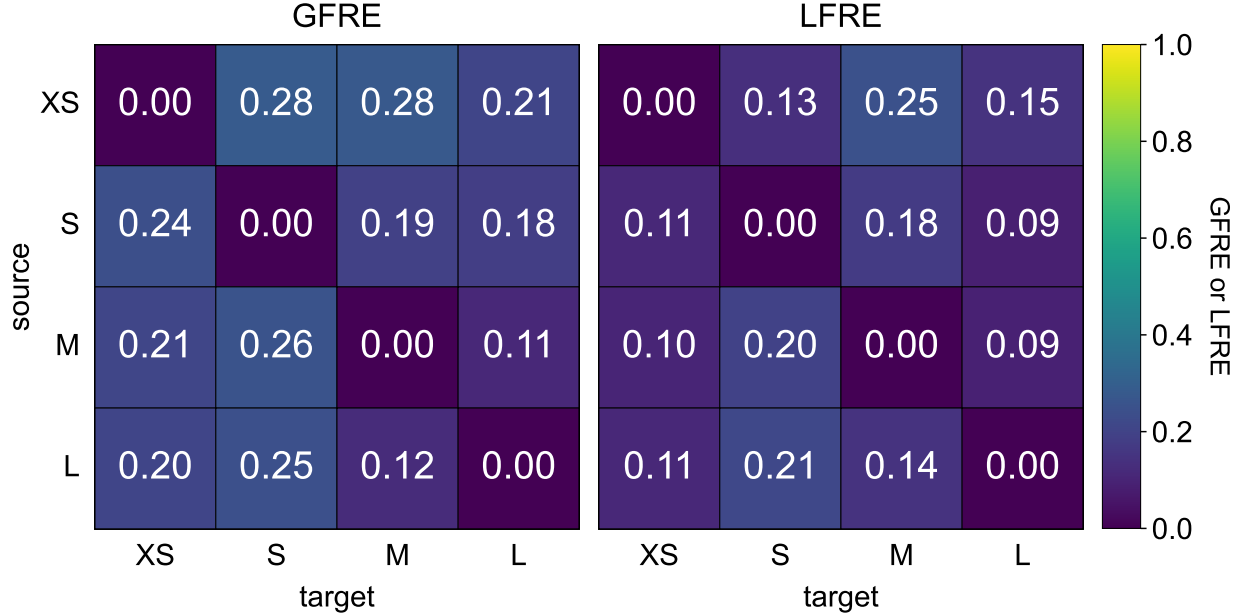


FIG. S7. Reconstruction errors across the PET-OMAT checkpoints of different sizes computed for the MAD test subset.

D. Single vs. multi-head architecture of the same model

We next compare the latent spaces of the single-head MACE-OMAT-0, the MACE architecture [10] fully trained on OMat24 [23] (MACE-OMAT-0), against the corresponding OMat24-specific readout head of the multi-head MACE-MH-1 model [11]. The multi-head variant is the MACE architecture enhanced with nonlinear interaction blocks and trained with multi-head replay fine-tuning, where task-specific readout heads are attached to a shared backbone and simultaneously trained on new data plus a replay buffer sampled from the original foundational training data to prevent catastrophic forgetting. As shown in Table S4, reconstruction is nearly symmetric with moderate GFRE but very low LFRE. This hints that the multi-head design preserves the local representational fidelity while enhancing the global readout. In other words, the latent feature space remains essentially unchanged locally, but globally, the newly devised training strategy allows the multi-head model to alter the manifold.

TABLE S4. GFRE and LFRE comparison between MACE-OMAT-0 (original MACE trained on OMAT) and MACE-MH-1-OMAT (OMAT head of the multi-head fine-tuned MACE model).

Reconstruction direction (source → target)	GFRE	LFRE
OMAT-0 → MH-1-OMAT	0.32	0.01
MH-1-OMAT → OMAT-0	0.35	0.1

IX. VARYING TARGETS

TABLE S5. GFRE and LFRE comparison between PET-MAD and PET-MAD-DOS.

Reconstruction direction (source → target)	GFRE	LFRE
PET-MAD → PET-MAD-DOS	0.68	0.39
PET-MAD-DOS → PET-MAD	0.56	0.28

Here, we evaluate the information content overlap between the last-layer features of PET-MAD (trained on energies and forces) and PET-MAD-DOS (trained on the electronic density of states) via feature reconstruction errors on the MAD test subset. The results show lower errors when reconstructing PET-MAD features from PET-MAD-DOS features compared to the reverse direction (Table S5). It indicates that the DOS-based features capture aspects sufficient for approximating energy-based features, while encoding additional information that the energy-only latent feature space may be oblivious to.

X. FINE-TUNING

A. Training errors and hyperparameters

The errors of each PET checkpoints corresponding to the different fine-tuning strategies have been evaluated on the test split of the LPS dataset composed of 412 structures. Results are shown in Table S6. We also report the hyperparameters used for the PET-based models in Table S7.

TABLE S6. Test set performance on LPS dataset for different PET-based models: PET-MAD, a pre-trained PET uMLIP baseline; BESPOKE, model trained from scratch; FF, model with full fine-tuning; HF, PET with head-only fine-tuning; FTL, model with full transfer learning training; HTL, model with head transfer learning.

Model	Energy	RMSE	Energy	MAE	Forces	RMSE	Forces	MAE
	(meV/atom)	(meV/atom)	(meV/Å)	(meV/Å)				
PET-MAD	210.01	208.26	129.69	75.95				
BESPOKE	4.19	2.44	99.71	51.23				
FF	8.73	6.58	89.44	54.59				
HF	8.57	6.98	96.30	58.28				
FTL	6.18	4.76	91.26	49.65				
HTL	8.70	7.17	98.10	58.44				

TABLE S7. Hyperparameters used for PET-based models across training strategies on the LPS dataset.

Parameter	Value
Cutoff (r_{cut})	4.5
NN width (d_{pet})	128
Number of GNN layers (N_{gnn})	2
Number of transformer layers (N_{tl})	2
Number of heads (N_{heads})	8
Learning rate	1×10^{-5}
Batch size	16

B. Latent space projection

In addition to the analyses in the main text, here we perform the PCovR analysis using the last-layer features extracted from PET checkpoints obtained with different fine-tuning techniques: full fine-tuning (FT), head fine-tuning (HF), full transfer learning (FTL), and head transfer learning (HTL) upon the LPS dataset. We also extract corresponding features from PET-MAD, which has been used as a pre-training basis. For the regression term of PCovR, we use the ground-truth cohesive energy, and we form the structure-level features by

using the second order cumulant or the concatenation of the mean and standard deviation of the atomic feature vectors. We set the mixing parameter $\alpha = 0.5$ to balance the regression and PCA terms, thereby enforcing consistency between checkpoint projections. Note that the PCovR space was first fitted using the embeddings from the MAD test subset, and the LPS projections were simply projected into this space.

The projections are consistent and similar across checkpoints, meaning that PET-derived representations retain the same global structure due to the common pre-trained backbone. We note that relatively larger fluctuations are observed for the transfer learning variants (FTL, HTL), which can be explained by the involvement of new heads with randomized initial weights. The similarities and differences observed in the PCovR projects are well-aligned with the global and local feature reconstruction errors presented in Section III A.

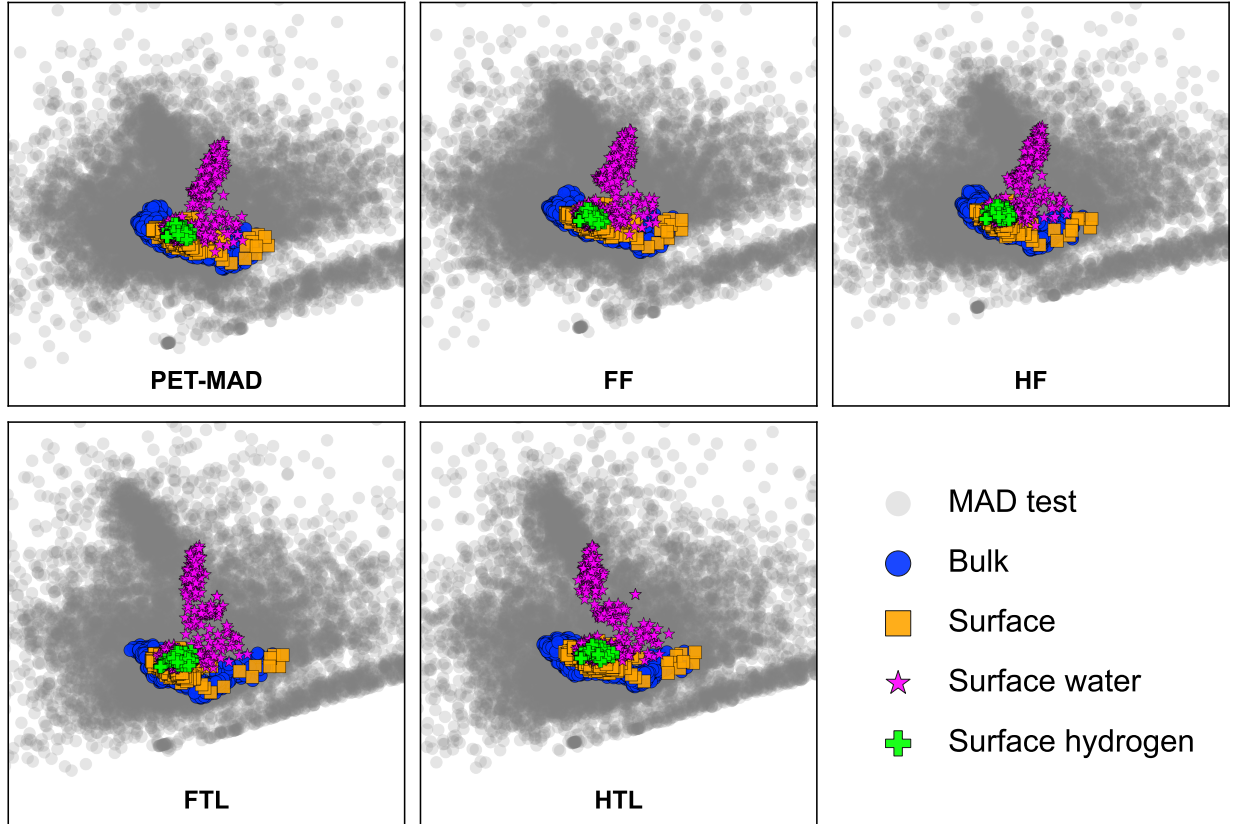


FIG. S8. Two-dimensional PCovR projections of the LPS dataset constructed using the last-layer features of PET checkpoints trained with different fine-tuning setups. The greyscale background points correspond to the test subset of the MAD dataset, and the colored points in each panel correspond to the PCovR projections of the LPS systems “within” the MAD latent space.

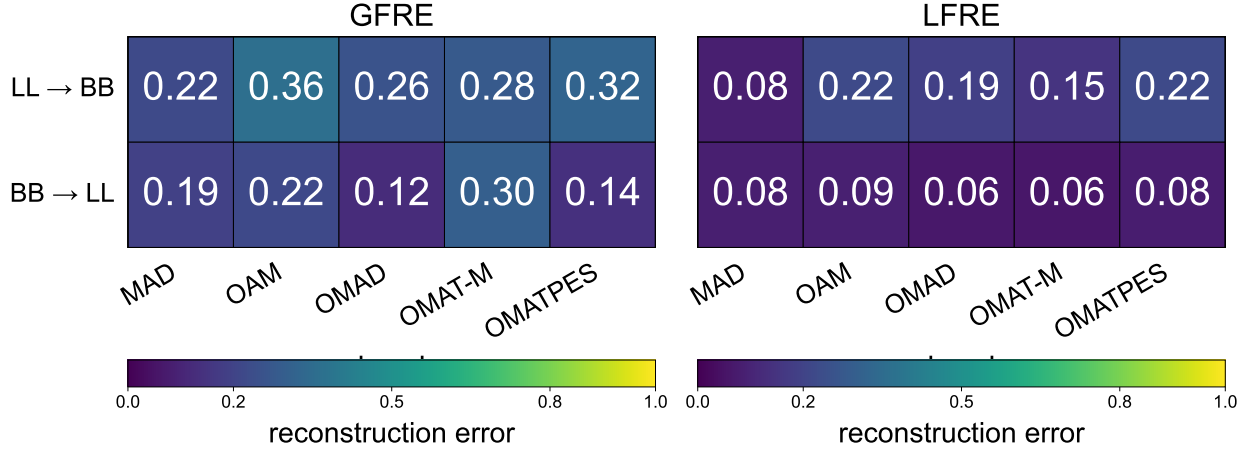


FIG. S9. Global and local reconstruction errors for the last-layer features (LL) and backbone features (BB) of different PET checkpoints computed for the MAD test dataset.

XI. BACKBONE VS. LAST-LAYER FEATURES

We compare backbone (BB) and last-layer (LL) features across five PET variants, described in SI VIII A 2. Checkpoints pre-trained on OMat24, corresponding to OAM, OMAD, OMAT, and OMATPES columns, show higher LL to BB reconstruction errors (Fig. S9) than the non-pre-trained MAD, which indicates that pre-training can enrich the BB features with transferable information. Overall, the flow is asymmetric, with an average GFREs of 0.29 for LL → BB and 0.19 for BB → LL, suggesting that BB features encode more information compared to the LL features.

XII. LOCAL TO GLOBAL FEATURES

The cumulants $\kappa_S^{(k)}$ are computed from the central moment $\mu_S^{(k)}$ as follows:

$$\kappa_S^{(1)} = \bar{\xi}_S^{(F)}, \quad (S1)$$

$$\kappa_S^{(2)} = \mu_S^{(2)}, \quad (S2)$$

$$\kappa_S^{(3)} = \mu_S^{(3)}, \quad (S3)$$

$$\kappa_S^{(4)} = \mu_S^{(4)} - 3(\mu_S^{(2)})^2, \quad (S4)$$

$$\kappa_S^{(5)} = \mu_S^{(5)} - 10\mu_S^{(2)}\mu_S^{(3)}, \quad (S5)$$

$$\kappa_S^{(6)} = \mu_S^{(6)} - 15\mu_S^{(2)}\mu_S^{(4)} - 10(\mu_S^{(3)})^2 + 30(\mu_S^{(2)})^3, \quad (S6)$$

$$\kappa_S^{(7)} = \mu_S^{(7)} - 21\mu_S^{(2)}\mu_S^{(5)} - 35\mu_S^{(3)}\mu_S^{(4)} + 210\mu_S^{(3)}(\mu_S^{(2)})^2, \quad (S7)$$

$$\kappa_S^{(8)} = \mu_S^{(8)} - 28\mu_S^{(2)}\mu_S^{(6)} - 56\mu_S^{(3)}\mu_S^{(5)} - 35(\mu_S^{(4)})^2 \quad (S8)$$

$$+ 420\mu_S^{(4)}(\mu_S^{(2)})^2 + 560(\mu_S^{(3)})^2\mu_S^{(2)} - 630(\mu_S^{(2)})^4. \quad (S9)$$

The global and local feature reconstruction errors across the uMLIPs computed with $\kappa_S^{(8)}$ are presented in Fig. S10.

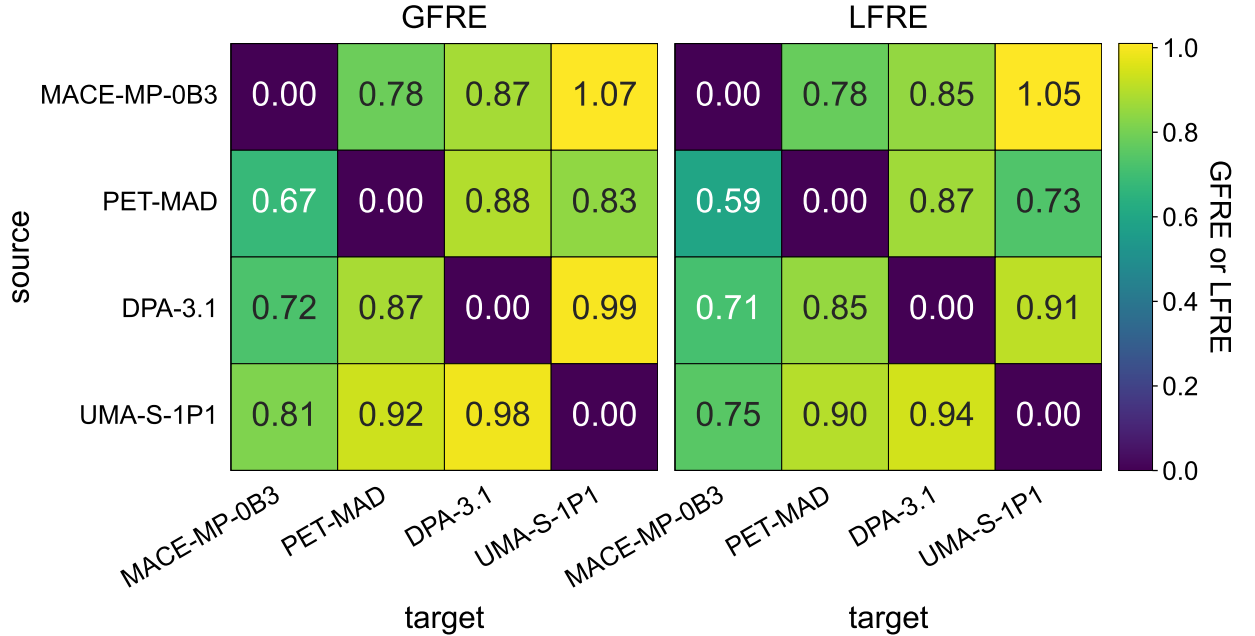


FIG. S10. Reconstruction errors of the eight-order cumulative structure-level features across the uMLIPs on the MAD test dataset.